Die approbierte gedruckte Originalversion dieser Diplomarbeit ist an der TU Wien Bibliothek verfügbar
The approved original version of this thesis is available in print at TU Wien Bibliothek.

TECHNISCHE UNIVERSITÄT WIEN

Diplomarbeit

Stabilization of MEMS-based Electric Field Sensor

ausgeführt zum Zwecke der Erlangung des akademischen Grades

Institut für Sensor- und Aktuatorsysteme
Technische Universität Wien

vorgelegt von:
Veljko Vukicevic
Matriculation number: 01528008

betreut von:
Ao. Univ. Prof. Dr. Franz Keplinger
Univ.Ass. Dipl.-Ing. Hajrudin Besic

Wien, am June 7, 2022

Die approbierte gedruckte Originalversion dieser Diplomarbeit ist an der TU Wien Bibliothek verfügbar
The approved original version of this thesis is available in print at TU Wien Bibliothek.

Eidesstattliche Erklärung

Ich erkläre an Eides statt, dass ich die vorliegende Masterarbeit selbstständig und ohne fremde Hilfe verfasst, andere als die angegebenen Quellen und Hilfsmittel nicht benutzt bzw. die wörtlich oder sinngemäß entnommenen Stellen als solche kenntlich gemacht habe.

Wien, June 7, 2022

Unterschrift (Author)

Die approbierte gedruckte Originalversion dieser Diplomarbeit ist an der TU Wien Bibliothek verfügbar
The approved original version of this thesis is available in print at TU Wien Bibliothek.
TU WIEN Bibliothek Your knowledge hub

Die approbierte gedruckte Originalversion dieser Diplomarbeit ist an der TU Wien Bibliothek verfügbar
The approved original version of this thesis is available in print at TU Wien Bibliothek.

Be prepared, work hard, and hope for a little luck. Recognize that the harder you work and the better prepared you are, the more luck you might have.

- Ed Bradley

Die approbierte gedruckte Originalversion dieser Diplomarbeit ist an der TU Wien Bibliothek verfügbar
The approved original version of this thesis is available in print at TU Wien Bibliothek.

Die approbierte gedruckte Originalversion dieser Diplomarbeit ist an der TU Wien Bibliothek verfügbar
The approved original version of this thesis is available in print at TU Wien Bibliothek.

Contents

Contents I

Abstract IV

Kurzfassung V

Acknowledgment VI

Introduction 1

1 Fundamentals 3
- 1.1 Electrostatics . . . 3
  - 1.1.1 Point Charge . . . 3
  - 1.1.2 Coulomb's Law . . . 3
  - 1.1.3 Electric Field . . . 4
  - 1.1.4 Gauss's law . . . 6
  - 1.1.5 Electrostatic Potential . . . 6
  - 1.1.6 Voltage . . . 7
  - 1.1.7 Energy in Electric Fields . . . 8
- 1.2 Mechanical Fundamentals . . . 10
- 1.3 Optical Readout . . . 12
- 1.4 State-of-the-art E-Field Measurement . . . 14
  - 1.4.1 Induction Sensors . . . 14
  - 1.4.2 Macroscopic Field Mill . . . 14
  - 1.4.3 MEMS Field Mill . . . 15
  - 1.4.4 Force Sensors . . . 17
  - 1.4.5 Passive Force Sensor . . . 17
  - 1.4.6 Active Force Sensor . . . 19

2 Implementation 23
- 2.1 MEMS Transducer . . . 24
- 2.2 PI Controller . . . 26
- 2.3 Main Board . . . 29
  - 2.3.1 Demodulation . . . 29
  - 2.3.2 ADC . . . 30
  - 2.3.3 Bias Electrodes Control . . . 31

Die approbierte gedruckte Originalversion dieser Diplomarbeit ist an der TU Wien Bibliothek verfügbar
The approved original version of this thesis is available in print at TU Wien Bibliothek.
TU WIEN Bibliothek Your knowledge hub

2.4 Microcontroller . . . 32
2.4.1 PI Controller Co-Routine . . . 33
2.4.2 Setpoint Co-Routine . . . 33
2.4.3 Round-trip Co-Routine . . . 34
2.5 Graphical User Interface Software . . . 35
2.5.1 Operating System and GUI Framework . . . 35
2.5.2 UART Communication . . . 35
2.5.3 Initialization and Warmup . . . 36
2.5.4 Main Window . . . 36

3 Results **39**
3.1 Drift . . . 39
3.2 PI Measurements . . . 41
3.3 Constant Bias Measurements . . . 45

Conclusion and Outlook **49**

Die approbierte gedruckte Originalversion dieser Diplomarbeit ist an der TU Wien Bibliothek verfügbar
The approved original version of this thesis is available in print at TU Wien Bibliothek.
TU WIEN Bibliothek Your knowledge hub

Die approbierte gedruckte Originalversion dieser Diplomarbeit ist an der TU Wien Bibliothek verfügbar
The approved original version of this thesis is available in print at TU Wien Bibliothek.

Abstract

The reliable and reproducible measurement of electrostatic fields has always represented a challenge, especially for lower frequencies smaller than 1 Hz. While today many physical quantities can be measured with micro- and nanosensors, no such sensor for DC and low-frequency electric fields exists on the market. Research mainly centers around MEMS-based sensors, typically MEMS field mills, but also force-based MEMS sensors.

This thesis deals with the stabilization of the DC field measurements with an active force sensor, by exploring two different stabilization approaches. In the first configuration, the drift was compensated by bias electrodes that were controlled through a control loop mechanism. The second configuration used a fixed bias voltage on the electrodes to shield the transducer from the charge build-up stemming from the ions accumulation on the dielectric materials in its proximity.

In the first configuration, the electrostatic drift could not be entirely compensated with the control loop. The system was then reconfigured with the goal of minimizing the amount of dielectric materials around the transducer and shielding all optical components. The reconfigured system was not showing the signs of electrostatic drift, so no stabilization was needed. However, the mitigation of ionic interference was still needed. This was achieved with a fixed voltage on the bias electrodes that shielded the transducer from the ions. The influence of different substrate materials is also interrogated and reported.

Die approbierte gedruckte Originalversion dieser Diplomarbeit ist an der TU Wien Bibliothek verfügbar
The approved original version of this thesis is available in print at TU Wien Bibliothek.
TU Bibliothek Your knowledge hub WIEN

Kurzfassung

Die zuverlässige und reproduzierbare Messung des elektrostatischen Feldes habt schon immer eine Herausforderung dargestellt, besonders für tiefere Frequenzen kleiner als 1 Hz. Während heute viele physikalische Größen mit Mikro- und Nanosensoren gemessen werden können, existiert kein Sensor für tieffrequente und statische elektrische Feldern am Markt. Die Forschung ist vor allem auf MEMS-basierte Sensoren fokussiert, meistens MEMS Feldmühlen aber auch kraftbasierten MEMS Sensoren.

Diese Arbeit behandelt die Stabilisierung der Messungen des Gleichfeldes mit einem aktiven kraftbasierten Sensor durch Untersuchung zweier Stabilisierungs-Ansätze. In der ersten Konfiguration wird die Drift über die Bias-Elektroden, die über einen Regelkreis gesteuert werden, kompensiert. Die zweite Konfiguration hat eine fixe Bias-Spannung verwendet, um den Wandler von der elektrostatischen Aufladung abzuschirmen, die von Ionen stammt, die sich auf das Dielektrikum in der Nähe des Wandlers anlagern.

In der ersten Konfiguration konnte die elektrostatische Drift nicht vollständig mit der Regelung kompensiert werden. Das System wurde daher rekonfiguriert, mit dem Ziel, so wenige Dielektrika wie möglich in der Nähe des Wandlers zu positionieren. Das rekonfigurierte System wies keine elektrostatische Drift mehr auf, daher war keine aktive Stabilisierung mehr nötig. Allerdings musste immer noch gegen die Effekte der Ionen vorgegangen werden. Dies wurde mit einer fixen Spannung an den Biaselektroden erzielt, die den Wandler von den Ionen abschirmt. Der Einfluss verschiedener Materialien des Substrats wurde auch untersucht und berichtet.

Die approbierte gedruckte Originalversion dieser Diplomarbeit ist an der TU Wien Bibliothek verfügbar
The approved original version of this thesis is available in print at TU Wien Bibliothek.
TU WIEN Bibliothek Your knowledge hub

Acknowledgment

Foremost, I would like to thank professor Franz Keplinger for the opportunity to work on this project. I would also like to thank Hajrudin Besic and Andreas Kainz for their constant guidance throughout the project, as well as Wilfried Hortschitz for his help and pleasant cooperation.

Special thanks to all the friends that made this journey fun and enjoyable.

I could not have undertaken this journey without my three sisters, Milica, Milena and Sonja that are always there for me. Words cannot express my gratitude to my parents, Slobodan and Dragana for their unlimited love and support that made all of this possible.

Die approbierte gedruckte Originalversion dieser Diplomarbeit ist an der TU Wien Bibliothek verfügbar
The approved original version of this thesis is available in print at TU Wien Bibliothek.
TU Bibliothek Your knowledge hub WIEN

Die approbierte gedruckte Originalversion dieser Diplomarbeit ist an der TU Wien Bibliothek verfügbar
The approved original version of this thesis is available in print at TU Wien Bibliothek.

Die approbierte gedruckte Originalversion dieser Diplomarbeit ist an der TU Wien Bibliothek verfügbar
The approved original version of this thesis is available in print at TU Wien Bibliothek.

Introduction

The electrostatic field is present all around us. The atmospheric electric field during clear weather is around $100 - 200\frac{\mathrm{V}}{\mathrm{m}}$ whereas during a thunderstorm the values are can be as high as tens of kilovolts per meter. This relation can be used to predict imminent lightning activity. Furthermore, HVDC (high voltage direct current) transmission lines create strong electric fields in their proximity. Measuring these low-frequency and static fields is very important for the better understanding of its influence on our health [2].

Measurement of the fields with such low frequencies is still a big technological challenge. Macroscopic field mills [3, 4] have been the industry standard for the longest time but they are prone to failure, have high power consumption and low spatial resolution. The MEMS based electric field mills (MEFM) [5–7] solved some of the problems, but the grounded shutter is affected by the higher fields which makes the measurement results unreliable.

Electrostatic force-based sensors show promising results, especially when actively driven at the resonance frequency such that a linear relation between the force and the electric field is achieved. One of the biggest challenges of this sensor design is the electrostatic drift that is caused by a static charge build-up on the dielectric materials in the proximity of the transducer, causing unreliable measurements. This can be caused either by the polarization effects of the dielectric itself or by ions from the environment.

This thesis is structured as follows: the first part covers the electromechanical fundamentals that cover the working principle of an active force-based sensor. Furthermore, state-of-the-art electric field sensors are discussed and finally the working principle of the sensor used in this project is explained. The second part is dedicated to the implementation of the sensor system from the transducer itself to the accompanying hardware used for signal processing and data acquisition. Lastly, two different drift stabilization approaches are discussed: a control loop mechanism that constantly compensates the external field and thus stabilizes the unwanted drift effect, and a constant bias voltage that shields the sensor from the charge build-up stemming from ions.

Die approbierte gedruckte Originalversion dieser Diplomarbeit ist an der TU Wien Bibliothek verfügbar
The approved original version of this thesis is available in print at TU Wien Bibliothek.
TU WIEN Bibliothek Your knowledge hub

Die approbierte gedruckte Originalversion dieser Diplomarbeit ist an der TU Wien Bibliothek verfügbar
The approved original version of this thesis is available in print at TU Wien Bibliothek.

Die approbierte gedruckte Originalversion dieser Diplomarbeit ist an der TU Wien Bibliothek verfügbar
The approved original version of this thesis is available in print at TU Wien Bibliothek.
TU WIEN Bibliothek Your knowledge hub

Chapter 1

Fundamentals

This chapter covers the basics of the electrical and mechanical forces upon which the MEMS functionality depends.

1.1 Electrostatics

Electrostatics is the study of the electric phenomena at rest and the electric fields that are generated by point charge or continuous time invariant charge distribution.

1.1.1 Point Charge

The assumption of a point charge is that the charged body is either sufficiently small or that it's dimensions are negligible compared to the reference system and that the body can be considered a single point in space. The SI unit of electric charge is Coulomb [C]. The charge of an object can be quantified as positive or negative and the interaction between the charges is described by Coulomb's law [8].

1.1.2 Coulomb's Law

At the core of electrostatics lies Coulomb's law. It states that the electrostatic force between two charged (point) bodies is proportional to the product of the charges and inversely proportional to the square of the distance between them [9]. It can be represented as:

$$\vec{F}_{21} = \frac{1}{4\pi\varepsilon_0}\frac{Q_1 Q_2}{r^2}\vec{e}_{21}, \tag{1.1}$$

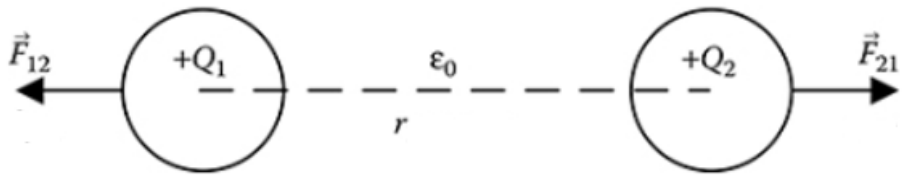

Figure 1.1: Electrostatic forces of two point charges Q_1 and Q_2 at a distance r in a vacuum (permittivity ε_0)

where Q_1 and Q_2 represent the charges of the two bodies that lie at distance r from one another, $\vec{F}_{21}$ is the force exerted by Q_1 on Q_2 and $\vec{e}_{21}$ is the unit vector in the direction of the force, which is pointed along the line connecting the two charges and in the direction from Q_1 to Q_2. The term $\frac{1}{4\pi\varepsilon_0}$ is a constant coefficient where ε_0 represents the permittivity of vacuum ($\varepsilon_0 \approx 10^{-9}/36\pi\frac{\mathrm{Nm}^2}{\mathrm{C}^2}$). In case of a different medium, additional relative permittivity ε_r is multiplied with the permittivity of the vacuum.

A body charge can be positive as well as negative, where the sign convention was introduced by American physicist and statesman Benjamin Franklin [8]. It is clear from Coulomb's Equation (1.1) that two bodies of the same charge polarity will create opposing forces, and two bodies of different polarity attracting forces between them. The case of two point charges of the same polarity is depicted in Fig. 1.1.

1.1.3 Electric Field

Coulomb's law can be expanded on arbitrary many bodies in space with the superposition principle. These two together can describe every electrostatic phenomena and they create the basis for the definition of the electric field [8]. For an arbitrary number of point charges N, the resulting force $\vec{F}(\vec{r})$ on a point charge Q at $\vec{r}$ (the position vector of the point charge in the reference system) in a vacuum (ε_0) can be represented as:

$$\vec{F}(\vec{r}) = \frac{1}{4\pi\varepsilon_0}\sum_{i=1}^{\mathrm{N}}\frac{QQ_i(\vec{r}-\vec{r}_i)}{|\vec{r}-\vec{r}_i|^3} \tag{1.2}$$

The electric field is then defined as the electric force per unit charge generated by arbitrarily displaced charged bodies in space. Since the electric field is generalized not only for positions where a charged body lies, but for every point in space, it is defined as force per unit charge

Die approbierte gedruckte Originalversion dieser Diplomarbeit ist an der TU Wien Bibliothek verfügbar
The approved original version of this thesis is available in print at TU Wien Bibliothek.
TU Bibliothek Your knowledge hub WIEN

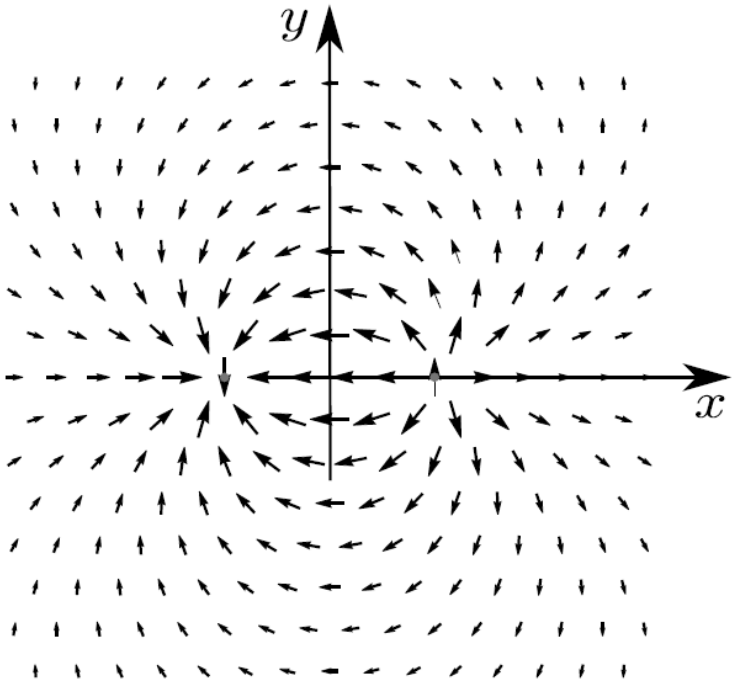

Figure 1.2: Vector plot of a dipole charge configuration [10]

of a small test charge Q_t [9]:

$$\vec{E} = \lim_{Q_t \to 0} \vec{F}/Q_t \tag{1.3}$$

The electric field intensity has the same direction and is proportional to the electric force. Its SI unit is volts per meter [V/m]. By substituting Eq. (1.1) in Eq. (1.3) and replacing the charge Q with the test charge Q_t, electrical field can also be formulated as:

$$\vec{E}(\vec{r}) = \frac{1}{4\pi\varepsilon_0} \sum_{i=1}^{\mathrm{N}} \frac{Q_i(\vec{r} - \vec{r}_i)}{|\vec{r} - \vec{r}_i|^3} \tag{1.4}$$

The electric field can be visualized using the vector field plot. It corresponds to placing of test charge on several points in space and calculating the electrical field in them. The electrical field direction is represented by the direction of an arrow and the magnitude is represented by its length [10]. An example of an electric field vector plot is depicted in Fig. 1.2

Die approbierte gedruckte Originalversion dieser Diplomarbeit ist an der TU Wien Bibliothek verfügbar
The approved original version of this thesis is available in print at TU Wien Bibliothek.
TU Bibliothek Your knowledge hub WIEN

1.1.4 Gauss's law

One of Maxwell's equations that is important for the measurement of electric fields is Gauss's law. It describes the relation between a charge and a resulting electric field. To describe this law, the quantity electric flux is introduced. The electric flux Φ is defined as:

$$\Phi = \int_{\mathrm{A}} \vec{E} \cdot \mathrm{d}\vec{A}, \tag{1.5}$$

where A represents an (imagined) closed surface and $\vec{E}$ is the electric field [8]. The derived SI unit most commonly used for the electric flux is volt meter [Vm]. Gauss's law states that the electrical flux through the closed surface A is proportional to the electric charge Q enclosed by that surface. The proportionality factor in the SI system is the permittivity of space, which is ε_0. This can be written as:

$$\int_{\mathrm{A}} \vec{E} \cdot d\vec{A} = \frac{Q}{\varepsilon_0} \tag{1.6}$$

1.1.5 Electrostatic Potential

The vector analysis of electrostatic fields can be very complex, whereas a scalar field would be much easier to handle. That is why the electrostatic potential φ is introduced. It is a scalar field that can be defined as

$$\varphi(\vec{r}) = \frac{1}{4\pi\varepsilon_0} \sum_{i=1}^{\mathrm{N}} \frac{Q_i}{|\vec{r} - \vec{r}_i|}, \tag{1.7}$$

where $\varphi(\vec{r})$ represents the electrostatic potential at $\vec{r}$ [8]. The terms are similar to the ones from the Eq. 1.4 and that is because the electric field and the potential are coupled through the relation

$$\vec{E}(r) = -\vec{\nabla}\varphi(r), \tag{1.8}$$

meaning that the electric field can be represented as the negative gradient of the electrostatic potential. It can be also physically interpreted as the potential energy per unit charge, whereas the electric field was defined as the force per unit charge. In other words, the potential represents the potential energy needed to overcome the electrostatic force of the electric field to bring the test charge to the point at $\vec{r}$ from infinitely far point, i.e. from the point where the electric field was zero.

Die approbierte gedruckte Originalversion dieser Diplomarbeit ist an der TU Wien Bibliothek verfügbar
The approved original version of this thesis is available in print at TU Wien Bibliothek.
TU Bibliothek Your knowledge hub WIEN

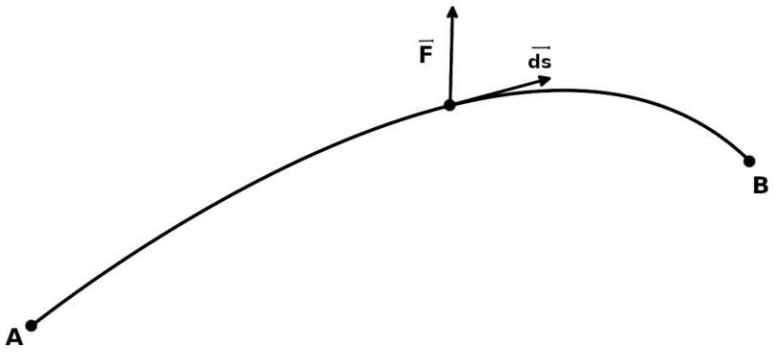

Figure 1.3: Force exerted on a body over a route between two points

1.1.6 Voltage

When outer forces act on a body, its displacement is connected with the form of energy we call work. Analogous to the work needed to displace a body inside a gravitational field, where the work is proportional to the body's mass, the displacement of a charged body is proportional to it's charge Q [11]. By moving a charge inside an electric field from point A to some point B (Fig. 1.3), its potential energy changes from W_A to W_B. This change of energy is proportional to the charge Q. In this way, the voltage is defined as the work needed to move a test charge between two points relative to its charge. Then the expression

$$U_\mathrm{BA} = \frac{W_\mathrm{B} - W_\mathrm{A}}{Q}, \tag{1.9}$$

represents the voltage between the points B and A. The work is represented in joules [J], whereas the unit for voltage is volt [V].

From the perspective of the force $\vec{F}$ needed to move the body between two points, the work W_BA can be represented as:

$$W_\mathrm{B} - W_\mathrm{A} = W_\mathrm{BA} = -\int_\mathrm{A}^\mathrm{B} \vec{F} \cdot \mathrm{d}\vec{s} \tag{1.10}$$

where $\mathrm{d}\vec{s}$ is an infinitesimal part of the displacement route. Inserting Equation (1.3) for the

Die approbierte gedruckte Originalversion dieser Diplomarbeit ist an der TU Wien Bibliothek verfügbar
The approved original version of this thesis is available in print at TU Wien Bibliothek.
TU Bibliothek Your knowledge hub WIEN

force brings the equation to the form:

$$W_{\mathrm{BA}} = -Q \int_{\mathrm{A}}^{\mathrm{B}} \vec{E} \cdot \mathrm{d}\vec{s} \tag{1.11}$$

Dividing both sides with the non-zero charge Q, using the Equation (1.9) and generalizing from two points to a arbitrary route s, the integral form of the voltage equation can be represented as:

$$U = \int_{\mathrm{s}} \vec{E} \cdot \mathrm{d}\vec{s} \tag{1.12}$$

The minus sign depends on the reference point and is only present if the integration starts from the reference point.

1.1.7 Energy in Electric Fields

As described in the previous section, moving the charge inside an electric field is connected with the (work) energy needed for its displacement. If we take a parallel plate capacitor with charges $+Q$ and $-Q$ on the plates respectively, the homogeneous electric field between the plates can be written as

$$E = \frac{U}{d} = \frac{Q}{C\,d}, \tag{1.13}$$

where the voltage across the capacitor can be represented as a fraction of the charge and the capacitance of the parallel plate capacitor [11]. The representation of electric field as a fraction of voltage over distance is a geometrical simplification of Equation (1.12) that is specific to a parallel plate capacitor. The distance between two plates is denoted as d (Fig. 1.4).

The work $\mathrm{d}W$ needed to transport an infinitesimally small charge $\mathrm{d}Q$ across the capacitor, assuming that the charge is so small that it doesn't change the electric field can be represented using the Equations (1.13), (1.3), (1.10) and the geometry simplifications of the parallel plates as:

$$\mathrm{d}W = F \cdot d = E \cdot \mathrm{d}Q \cdot d = \frac{Q}{C} \cdot \mathrm{d}Q \tag{1.14}$$

and in order to fill up the whole capacitor to a charge Q_{e}, the work has to be integrated:

$$W_{\mathrm{e}} = \int_0^{Q_e} \mathrm{d}W = \frac{1}{C} \cdot \int_0^{Q_e} Q \cdot \mathrm{d}Q = \frac{Q_{\mathrm{e}}^2}{2C} \tag{1.15}$$

This work is stored inside the capacitor and we say that it is holding electric energy. The

Die approbierte gedruckte Originalversion dieser Diplomarbeit ist an der TU Wien Bibliothek verfügbar
The approved original version of this thesis is available in print at TU Wien Bibliothek.
TU Bibliothek Your knowledge hub WIEN

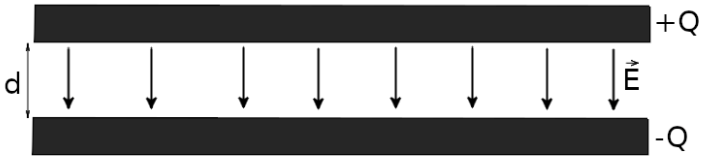

Figure 1.4: Parallel plate capacitor represented in 2D. Opposite charges Q create a homogeneous E-field across the distance d

energy inside a capacitor can be then represented generally as

$$W_\mathrm{e} = \frac{1}{2}\frac{Q^2}{C} = \frac{1}{2}C\,U^2 = \frac{1}{2}Q\,U \tag{1.16}$$

This energy is not material dependent and it can also exist inside a vacuum, meaning the energy exists wherever an electric field exists.

Energy is often represented through energy density w_e which is represented in joule pro cubic meter [J/m^3]. Simplified for a parallel plate capacitor, the energy density can be represented as

$$w_\mathrm{e} = \frac{W_\mathrm{e}}{V} = \frac{\frac{1}{2}C\,U^2}{A\,d} = \frac{\frac{1}{2}\varepsilon\frac{A}{d}(E\,d)^2}{A\,d} = \frac{1}{2}\varepsilon E^2, \tag{1.17}$$

where ε represents the permittivity of the dielectric material inside the capacitor and A is the area of the plate. Using the definition of electric displacement field:

$$D = \varepsilon E, \tag{1.18}$$

the energy can be rewritten as

$$w_\mathrm{e} = \frac{1}{2}\varepsilon E^2 = \frac{1}{2}\frac{D^2}{\varepsilon} = \frac{1}{2}D\,E. \tag{1.19}$$

The energy density can then be integrated over the arbitrary volume to calculate the energy of the electric field that it holds

$$W_\mathrm{e} = \int_V w_\mathrm{e} \cdot \mathrm{d}V \tag{1.20}$$

Die approbierte gedruckte Originalversion dieser Diplomarbeit ist an der TU Wien Bibliothek verfügbar
The approved original version of this thesis is available in print at TU Wien Bibliothek.
TU Bibliothek Your knowledge hub WIEN

1.2 Mechanical Fundamentals

As the MEMS abbreviation stands for "micro-electromechanical system", the mechanical aspect plays a big role and it is tightly coupled with the electrostatic forces explained in the previous chapter. Coulomb's force Eq. (1.4) acts upon the compliant elements of the transducer and creates a spatial displacement. When the electrostatic force is harmonic, the transducer's oscillation can be modelled as a damped driven linear resonator with one degree of freedom [12]. The corresponding equation of motion is a second order linear differential equation and can be written as

$$m\ddot{z} + c\dot{z} + kz = F(t), \tag{1.21}$$

where m is the mass of the moving element, c is the damping coefficient, k is the spring constant, z is the displacement and $F(t)$ is the driving force. The sinusoidal driving force comes from the voltage that is applied and as shown in Equation (1.3) the voltage is coupled with the charge on the charge is directly proportional to the force exerted. If we rewrite the force as

$$F(t) = F_0 \cos(\omega t), \tag{1.22}$$

the stationary solution of Eq. (1.21) can be represented as

$$z(t) = z_0 e^{(i\omega t)}, \tag{1.23}$$

and by substituting this back in Eq. (1.21) the complex amplitude z_0 can be written as

$$z_0 = \frac{F_0/m}{(\omega_0^2 - \omega^2) + 2i\,\zeta\,\omega_0\,\omega}, \tag{1.24}$$

where ζ is the damping ratio

$$\zeta = \frac{c}{2\sqrt{k\,m}}, \tag{1.25}$$

and ω_0 is the eigenfrequency of the free undamped system

$$\omega_0 = \sqrt{\frac{k}{m}}. \tag{1.26}$$

The eigenfrequency of the oscillator is the frequency at which the system oscillates without any driving or damping force. In this case, the system also has the highest amplitude at its

Die approbierte gedruckte Originalversion dieser Diplomarbeit ist an der TU Wien Bibliothek verfügbar
The approved original version of this thesis is available in print at TU Wien Bibliothek.
TU Bibliothek Your knowledge hub WIEN

eigenfrequency. This position of the amplitude's maximum is called resonance frequency ω_r and it is located at $\partial z/\partial\omega = 0$. For a damped system with no driving force ($F = 0$), the eigenvalues of the system can be represented as

$$\gamma_{1,2} = -\omega_0 \left(\zeta \pm \sqrt{\zeta^2 - 1}\right). \tag{1.27}$$

We can differentiate between 3 cases depending on the damping ratio. If $\zeta > 1$ the amplitude experiences an exponential decay, for $\zeta = 1$ the system is critically damped and the oscillation stops in the least amount of time and for $\zeta < 1$ the solution becomes imaginary and it exhibits oscillation. It can be observed from Eq. (1.27) that when the damping ratio is low ($\zeta \ll 1$), the resonance frequency and eigenfrequency (imaginary part of Eq. (1.27)) are approximately the same.

Furthermore we can define a quality factor Q that represents the ratio between the maximal energy stored in the system and the energy lost in the one radian cycle of oscillation. It can be approximated as

$$Q = \frac{1}{2\zeta}, \tag{1.28}$$

for the low damping ratio.

The bode diagram for different quality factor is depicted in Fig. 1.5. A higher quality factor corresponds to a steeper amplitude response and thus allows for higher sensor sensitivity. That's why it is desired to keep the MEMS transducer at its resonance frequency for more precise measurements.

Die approbierte gedruckte Originalversion dieser Diplomarbeit ist an der TU Wien Bibliothek verfügbar
The approved original version of this thesis is available in print at TU Wien Bibliothek.
TU Bibliothek Your knowledge hub WIEN

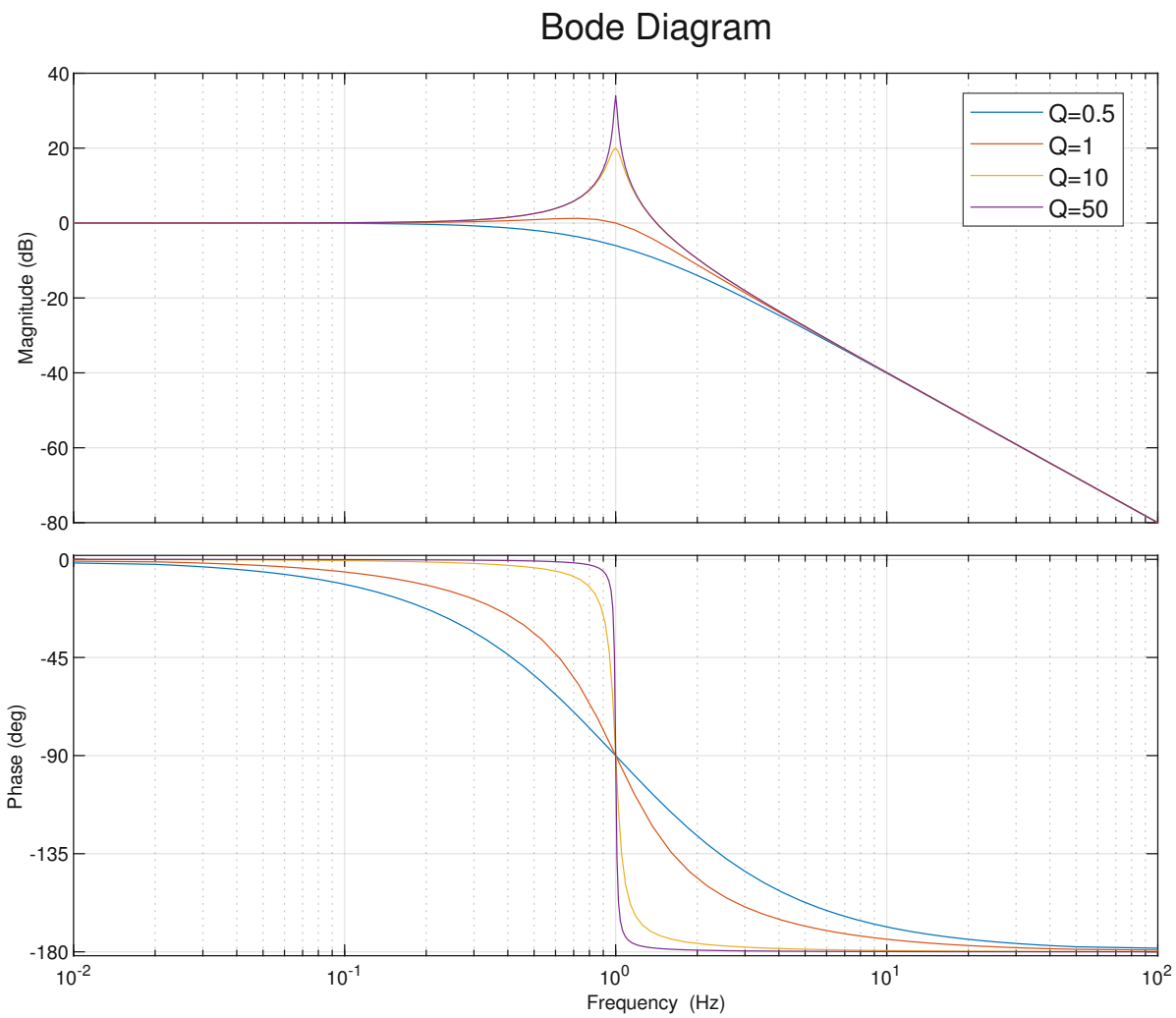

Figure 1.5: Bode diagram of the amplitude z_0 from Eq. (1.24) for different Q factors

1.3 Optical Readout

The force derived above creates a displacement of the moving part of the MEMS, which depends on the E-field to be measured. The remaining task is to determine the displacement. The readout of the MEMS displacement is an additional challenge, especially in micromachined sensors where the smallest interference can lead to faulty measurement results. That's why an optical readout has a big advantage since it is not interfering with the electric field (in the measuring spectrum) [13]. To measure the displacement discussed in Section 1.2 an optical interferometer can be used. The first implementation was reported in 1997 [14] where a Fabry-Pérot-Interferometer was used. The optical readout of the MEMS E-field

Die approbierte gedruckte Originalversion dieser Diplomarbeit ist an der TU Wien Bibliothek verfügbar
The approved original version of this thesis is available in print at TU Wien Bibliothek.
TU Bibliothek Your knowledge hub WIEN

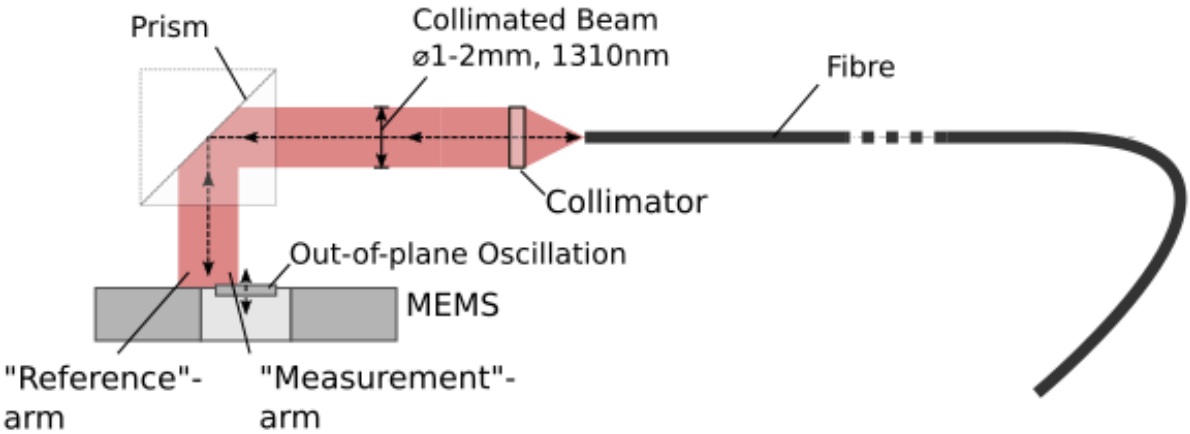

Figure 1.6: Common path interferometer working principle

sensor started receiving more attention in the last decade with the further development of the MEMS sensors. Instead of the previously used etalon, newer researches report the use of a highly sensitive aperture that is mounted on the chip, lowering the volume of the sensor significantly [15, 16].

Also, other interferometry method than the mentioned Fabry-Pérot-Interferometer can be used. This includes Laser Doppler vibrometer, Michelson interferometer or a common path interferometer. The common path interferometer has the advantage that the reference beam and the sample beam travel along the same path, reducing the possibility of interference. This way an active stabilization of the phase of the Michelson interferometer is not necessary. However, this comes at the cost of increased complexity of the MEMS. A diagram of the common path interferometer used in this project is depicted in 1.6. The reference and the measurement beam are first collimated, then they both travel the same path and are guided onto the MEMS using a prism. The function of this interferometer is out of the scope of this thesis thus it is only shortly explained here.

Die approbierte gedruckte Originalversion dieser Diplomarbeit ist an der TU Wien Bibliothek verfügbar
The approved original version of this thesis is available in print at TU Wien Bibliothek.
TU Bibliothek Your knowledge hub WIEN

1.4 State-of-the-art E-Field Measurement

1.4.1 Induction Sensors

The most conventional E-Field sensors are based upon the electric induction that can be derived from Gauss's law Eq. (1.6) if we rewrite it as:

$$Q = \varepsilon_0 E A, \tag{1.29}$$

where A represents the closed surface around the charge Q. The dot product is simplified to simple multiplication by assuming a right angle between the surface and the electrical field. The induced current is then the change of the charge Q through time or time derivation of charge:

$$I = \frac{\partial Q}{\partial t} = \varepsilon_0(\dot{E}A + E\dot{A}) \tag{1.30}$$

In order to measure the current, a variation of charge over time is needed. Since a DC electric field creates a constant charge distribution, the field mill sensor creates a variation either by periodically shielding the sensing electrodes ($\dot{A}$) or by moving a grounded shutter in the proximity of the electrodes so that some of the field lines that were going into the sensing electrode now terminate in the shutter and then go back into the sensing electrode when the shutter moves further away ($\dot{E}$).

1.4.2 Macroscopic Field Mill

The electric field mill is based on Equation (1.30) where the surface A changes over time ($A(t)$). The induced current is proportional to the surface area of the sensing probe that is exposed to the electric field [4]. The area can either change by rotating the electrodes so that they are periodically exposed to the field (cylindrical field mill) or by rotating the shutter above the electrodes (rotating shutter). The rotating shutter field mill is the most common form of this sensor and is depicted in Fig. 1.7.

Even though less used, the cylindrical field mill has the advantage of additional information about the field direction that can be acquired from the phase shift between the measured signal and the electric field. The rotating shutter field mill has to be oriented in the direction of the field (electrodes are normal to the electric field) for it to measure the maximal magnitude.

When both the electrodes and the shutter wings are symmetrical sectors like in Fig. 1.7,

Die approbierte gedruckte Originalversion dieser Diplomarbeit ist an der TU Wien Bibliothek verfügbar
The approved original version of this thesis is available in print at TU Wien Bibliothek.
TU Bibliothek Your knowledge hub WIEN

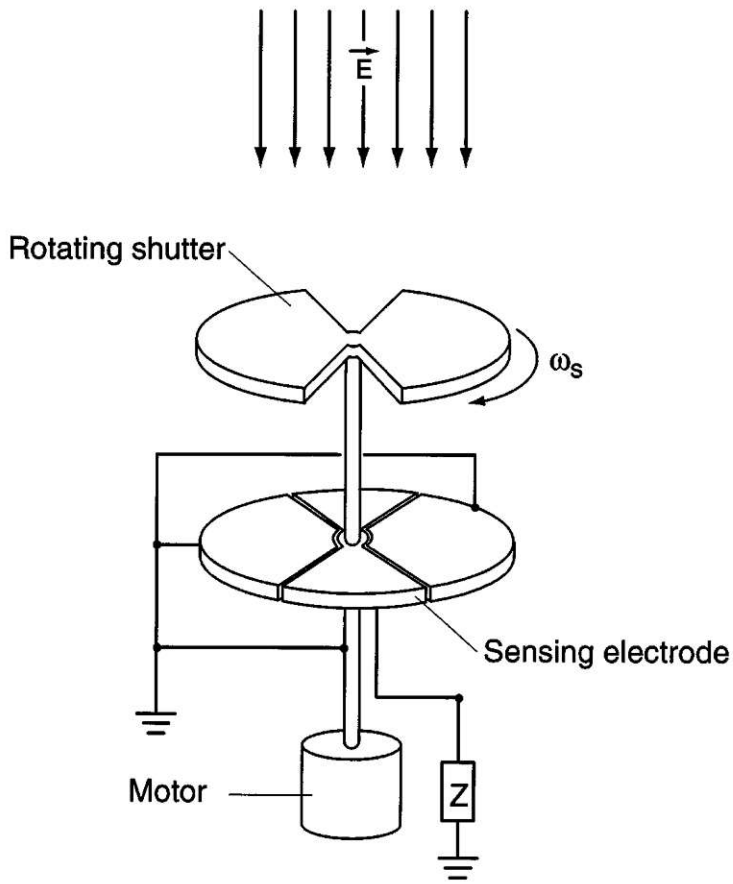

Figure 1.7: Shutter-type electric field mill for measurement of the magnitude of an electrostatic field [4]

the function of exposed area over time $A(t)$ will be a triangular function [3]. The induced charge in the sensing electrodes is directly proportional to the area so it will also create a triangular function $Q(t)$. The induced current is a time derivative of the charge Equation (1.30) and the result of differentiating a constant slope triangular function is a square function. Figure 1.8 depicts this relation between the area and the induced current $I(t)$ that is measured by the sensor.

1.4.3 MEMS Field Mill

Sensor technology is aiming for smaller and more efficient sensors. Macroscopic field mills are unable to measure fine spatial resolution of the field but furthermore also suffer from motor wear, high power consumption and are more prone to failures [5]. This has lead to the development of micro-mechanical field mills.

Die approbierte gedruckte Originalversion dieser Diplomarbeit ist an der TU Wien Bibliothek verfügbar
The approved original version of this thesis is available in print at TU Wien Bibliothek.
TU WIEN Bibliothek Your knowledge hub

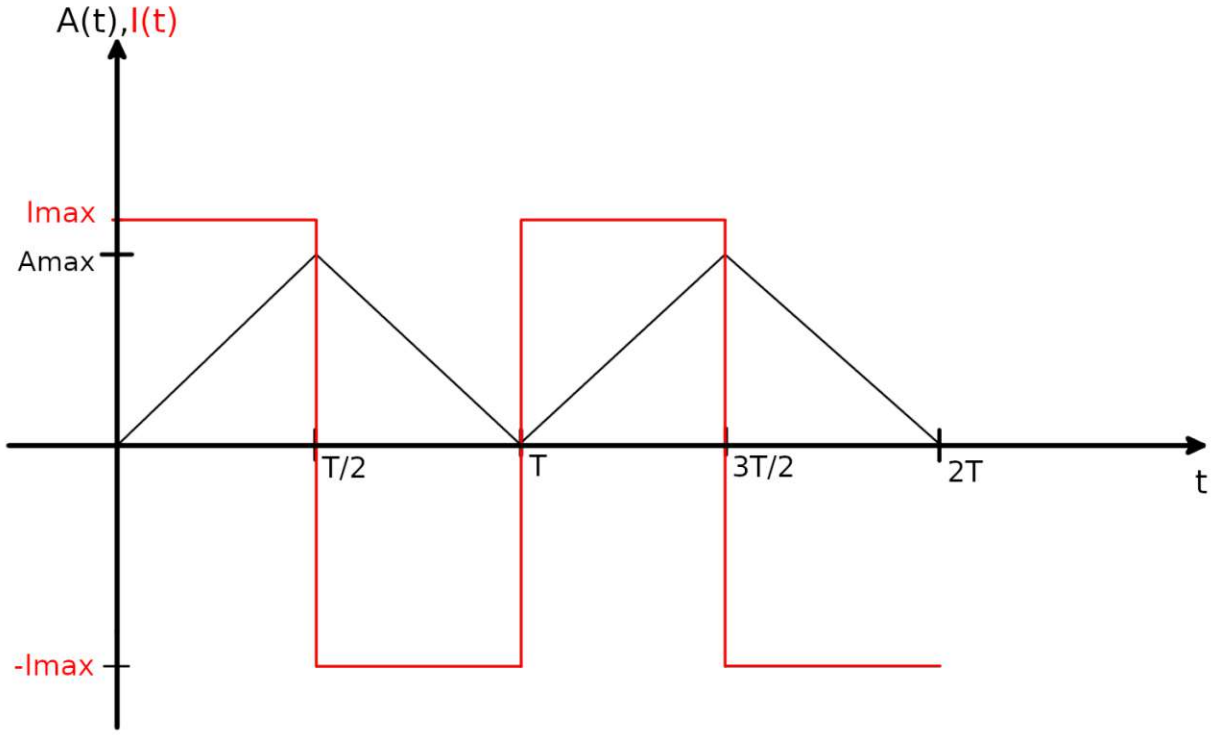

Figure 1.8: Waveforms of area $A(t)$ and measured current $I(t)$ of the field mill

Instead of rotating shutter blades that are hard to fabricate on a microscopic level, MEMS field mills use comb shaped moving shutters. The lateral movement of the shutter can either completely cover the sensing electrodes [6] or oscillate between positive and negative sensing electrode, pulling more electric field lines towards itself [5]. The non-covering shutter is depicted in Fig. 1.9. The shutter movement is achieved by actuator electrodes that create an electrostatic force acting upon the grounded shutter. In the case of a non-covering shutter, the positive and negative electrode comb is placed in a way that in its leftmost position, the shutter is closer to the positive electrode, covering its side walls and in its rightmost position the shutter is closer to the negative electrode.

The electrostatic actuation is easy to implement but it creates a parasitic feedthrough capacitance that couples with the measuring signal [7]. This can be reduced by differential sensing as shown in Fig. 1.9. Instead of one sensing electrode, a pair of positive and negative sensing electrodes is used that are then connected to a differential amplifier. This way the parasitic capacitance that acts upon both electrodes is reduced and the signal to noise ratio is improved.

Die approbierte gedruckte Originalversion dieser Diplomarbeit ist an der TU Wien Bibliothek verfügbar
The approved original version of this thesis is available in print at TU Wien Bibliothek.
TU Bibliothek Your knowledge hub WIEN

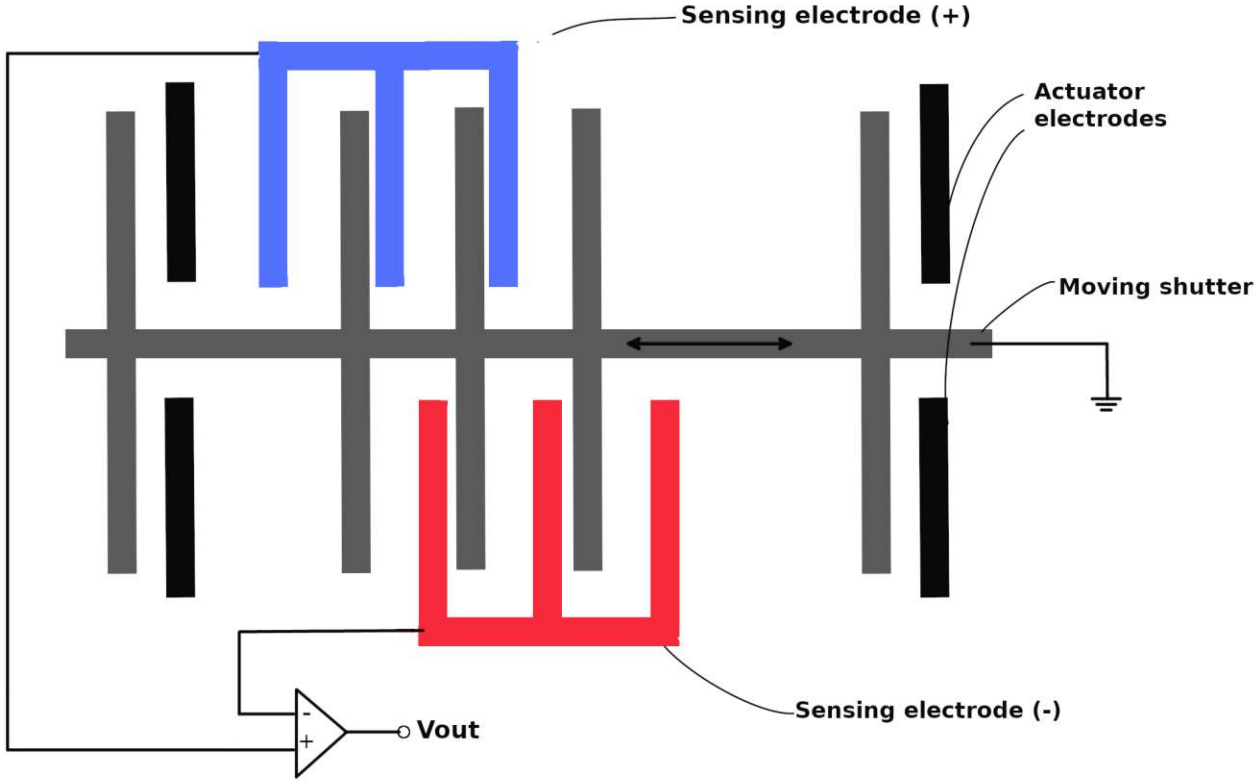

Figure 1.9: MEMS Field mill working principle with non-covering moving shutter

1.4.4 Force Sensors

Force sensors are based on Coulomb's force Eq. (1.1) where the force that acts on charges is created by the electric field that is to be measured Eq. (1.3). The micro-machined transducers as described in Section 1.2 transform the force in a displacement of a cantilever-like structure.

1.4.5 Passive Force Sensor

The working principle of the passive force sensors exploits the electrostatic induction effect, where a conducting body when placed inside an electric field experiences polarization and creates two oppositely charged regions on its surface [13]. These sensors can be seen as passive because the net charge of the body remains $Q = 0$ and there is no driving element to additionally charge the conductor. The conducting body is able to produce these two charged regions thanks to the free charge carriers and their mobility inside conductor's lattice while they try to compensate the outer electric field. This microscopic effect can

Die approbierte gedruckte Originalversion dieser Diplomarbeit ist an der TU Wien Bibliothek verfügbar
The approved original version of this thesis is available in print at TU Wien Bibliothek.
TU WIEN Bibliothek Your knowledge hub

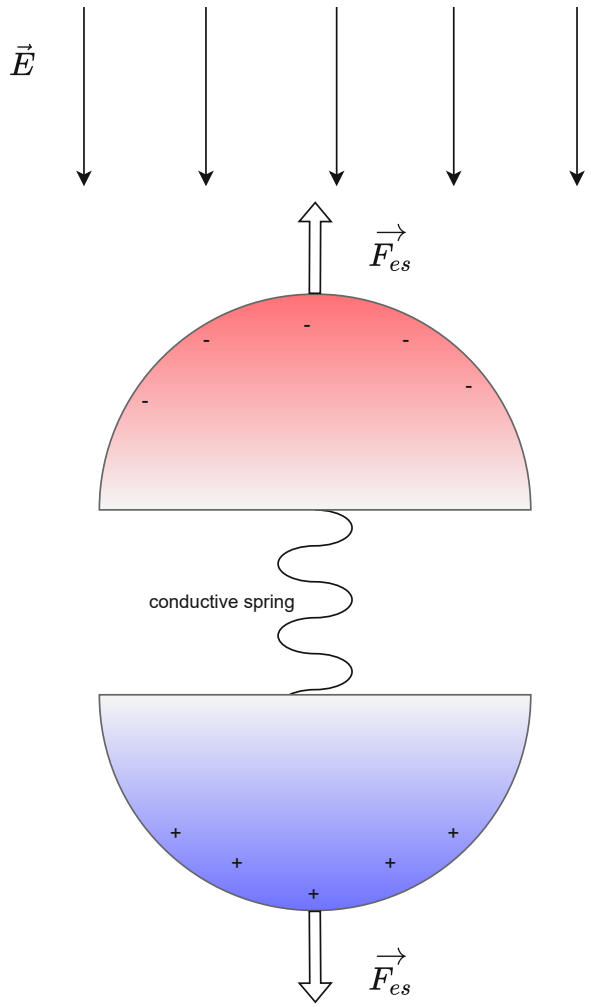

Figure 1.10: Two oppositely charged regions of the sphere in an electric fields connected with a conductive spring

also be explained through polarization $\vec{P}$ that simultaneously describes the induced electric dipole moment in a dielectric material as well as the microscopic response of a body on the applied electric field. The relation between polarization $\vec{P}$, electric field $\vec{E}$ and electric flux density $\vec{D}$ is

$$\vec{D} = \varepsilon_r \varepsilon_0 E = (1 + \chi)\varepsilon_0 E = \varepsilon_0 E + P, \tag{1.31}$$

where ε_r is the relative permittivity and $\chi = \varepsilon_r - 1$ is the electric susceptibility [9]. This equation shows that materials with high relative permittivity are strongly polarized inside an electric field and ideal conductors ($\varepsilon_r \to \infty$) are completely polarized.

If we observe a sphere inside an electric field that experiences this effect of oppositely

Die approbierte gedruckte Originalversion dieser Diplomarbeit ist an der TU Wien Bibliothek verfügbar
The approved original version of this thesis is available in print at TU Wien Bibliothek.
TU Bibliothek Your knowledge hub WIEN

charged surface charges and we split the sphere in half with a conducting spring connecting the two halves, we can observe an elongation of the spring [15] (Fig. 1.10). This elongation comes from the electrostatic force $\vec{F}_{\text{es}}$ that acts on the two halves of the sphere in opposite directions. Since the two force vectors are of the same intensity and opposite direction, the overall force is 0, as is the charge. In the MEMS implementation the conducting body consists of a doped silicon spring-suspended part and its relative displacement depends on the the measured electric field. The displacement can be modelled according to the lumped parameter model model described in Section 1.2. The force depends linearly on the electric field and the polarization. Since the polarization also depends on the electric field (microscopic response to the electric field), the force is overall proportional to the squared electric field $F_{\text{es}} \propto E^2$. This means that only the absolute value of the electric field can be measured and not its direction (i.e., the sign).

The displacement of the moving part of the MEMS is measured using an optical readout for the reason discussed in Section 1.3

1.4.6 Active Force Sensor

The sensor used for measurements in this thesis can be categorized as an active force sensor in accordance with the categorization from Section 1.4. It's underlying principle is similar to the passive sensor from Subsection 1.4.5 in that the displacement of the MEMS cantilever comes from the electrostatic force, however the disadvantage of the passive system is that it is sensitive to acoustic and electromagnetic noise. This is avoided by driving the MEMS at its resonance frequency and reading out the modulated measurement signal [17–19].

Force Derivation

To derive the electrostatic force that acts on the cantilever, we model the system as a parallel plate capacitor from Subsection 1.1.7. The cantilever itself is not an ideal parallel plate capacitor, but it can be modelled as such for the sake of simplicity. As we derived the energy stored in the capacitor in Equation (1.16), we can rewrite it as:

$$W = \frac{1}{2} C U^2 = \frac{1}{2} \frac{\varepsilon A}{d} (E\,d)^2 = \frac{1}{2} \varepsilon A E^2 d \tag{1.32}$$

where d represents the distance between the two plates (in the direction of z-axis) and $\varepsilon = \varepsilon_0 \varepsilon_{\text{r}}$ is absolute permittivity of the material. We can represent the force as a negative

Die approbierte gedruckte Originalversion dieser Diplomarbeit ist an der TU Wien Bibliothek verfügbar
The approved original version of this thesis is available in print at TU Wien Bibliothek.
TU Bibliothek Your knowledge hub WIEN

gradient of the energy as:

$$F = -\nabla W = -\frac{1}{2}\varepsilon A\, E^2 = -\frac{1}{2}\varepsilon A \left(\frac{U}{d}\right)^2 \tag{1.33}$$

under the assumption that the electric field is homogeneous and pointing in the direction of the z-axis [20]. Since the MEMS is driven with a sinusoidal voltage that generally can contain an additional DC component $U_{\text{drive}} = U_{\text{DC}} + U_0 \sin(\omega t)$ at the resonance frequency and the outer electrostatic field to be measured creates an additional voltage U_{out}, the resulting voltage on the cantilever can be represented as the voltage difference between the outer E-field voltage and the driving voltage and inserted in Eq. (1.33) as

$$F = -\frac{1}{2}\varepsilon A \left(E - \frac{U_{\text{drive}}}{d}\right)^2 = -\frac{1}{2}\frac{\varepsilon A}{d^2}\left(E^2 d^2 - 2EU_{\text{drive}}d + U_{\text{drive}}^2\right) \tag{1.34}$$

The voltage components can be observed in Eq. (1.34): the square of the field to be measured, the fundamental frequency component and the second harmonic. Whereas the square of the field and the second harmonic have a non-linear dependency on the field, the middle term has a linear relationship [17]. It represents the electric field to be measured but modulated at the resonance frequency (which is the driving frequency of U_{drive}) of the MEMS. This electrostatic force then creates a spatial displacement that is measured through an optical readout. The advantage of this approach is that the signal-to-noise ratio can be reduced through the modulation and a lock-in amplifier at the resonance frequency.

Modulation

The modulation of the E-field in the middle term of Eq. 1.34 can be visually represented in the frequency spectrum for better understanding (Fig. 1.11). The sinusoidal driving voltage creates two images symmetrical about the y-axis and with an f_{drive} offset from the original spectrum. This means that the highest frequency component of the electric field to be measured has to be two times smaller than the driving (resonance) frequency of the transducer in order to avoid the overlap between the original and the modulated spectrum. This can be achieved with a low-pass filter with a cut-off frequency f_c that eliminates all higher frequencies from the measuring signal. An ideal low-pass filter would create an abrupt cut-off resulting in a frequency spectrum in a shape of a rectangle, but in practice, the low-pass cuts the frequencies that are just over the cut-off threshold much less than the higher frequencies. This results in a frequency spectrum that can be modelled as a trapezoid,

Die approbierte gedruckte Originalversion dieser Diplomarbeit ist an der TU Wien Bibliothek verfügbar
The approved original version of this thesis is available in print at TU Wien Bibliothek.
TU Bibliothek Your knowledge hub WIEN

where the frequency at which the spectrum actually falls to 0 can be denoted as $f_{\max}$ as the maximal frequency component of the spectrum. The two cases depicted in Fig. 1.11a shows the minimal requirement for no overlapping ($f_{\text{drive}} = 2f_{\max}$) and in Fig. 1.11b, the case where this condition is violated and the spectrums overlap ($f_{\text{drive}} < 2f_{\max}$). In practice, it is desired that the gap between the spectrums is bigger, so an actual condition is $f_{\text{drive}} > 2f_{\max}$.

The higher resonance frequency also allows for broader bandwidth of the signal. The Eq. 1.26 shows that the resonance frequency of the oscillator can be increased either by lowering the mass, which is unpractical, or by increasing the spring constant k, which lowers the amplitude of the displacement. This is an important trade-off because higher k means higher bandwidth but lower deflection amplitudes, i.e. lower sensitivity.

the forces that act upon the cantilever are approx. several piconewtons [13] so the higher amplitude is crucial and the higher resonance frequency allows for a wider measuring bandwidth.

Drift

One of the biggest challenges with the electrostatic force sensors is their vulnerability to different environmental factors that can cause measurement errors. Any charges in the MEMS proximity influence the resulting electrostatic force and thus lead to measurement errors that can be observed as a drift in the measured signal from the expected value. When it comes to dielectric materials, there are several unwanted properties that have to be taken into account [22]:

- Current leakage directly through the material.
- Current leakage over the surface of the material, which is mostly coupled with surface contamination.
- Current leakage caused by absorbed water inside the insulator
- Charge unbalance by the water film on the material's surface
- Charge unbalances by charge stored inside the material (caused by a mechanical stress/ piezoelectric effect).
- Charge unbalances due to triboelectric effects (friction against other materials).
- General dielectric absorption where the material stores and releases charges over time.

Die approbierte gedruckte Originalversion dieser Diplomarbeit ist an der TU Wien Bibliothek verfügbar
The approved original version of this thesis is available in print at TU Wien Bibliothek.
TU WIEN Bibliothek Your knowledge hub

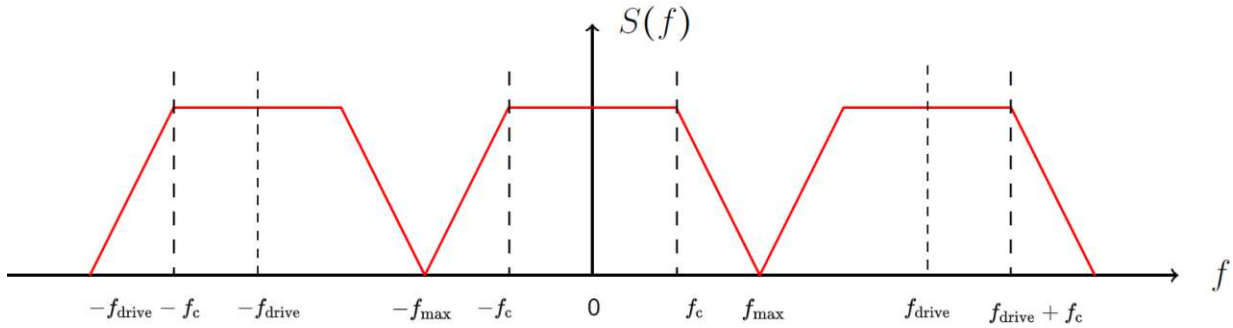

(a) $f_{\text{drive}} = 2f_{\text{max}}$

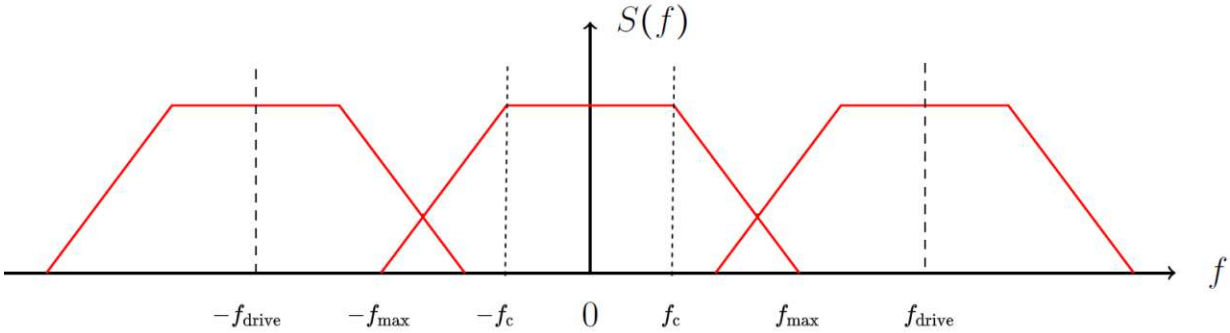

(b) $f_{\text{drive}} < 2f_{\text{max}}$

Figure 1.11: Frequency spectrum of the original signal (middle trapezoid) and the modulated signal (two outer ones) for the border case (a) and the spectrum interference(b) (modified from [21])

One of the most commonly used dielectric materials is Teflon because of its very high resistivity, hydrophobicity and chemical inertia. On the other hand it is known to produce unwanted voltages and leakage currents under impurities caused by deformation.

The issue is especially noticeable in ionic environments, such as in the proximity of the HVDC transmission lines, where a large number of ions lands on the dielectric material, creating a charge unbalance. This effect can be mitigated by applying a fixed bias voltage that deflects the incoming ions [23] or by implementing an actuator system that actively compensates the electric field locally. The approaches used in this project will be explained in later chapters.

Die approbierte gedruckte Originalversion dieser Diplomarbeit ist an der TU Wien Bibliothek verfügbar
The approved original version of this thesis is available in print at TU Wien Bibliothek.
TU Bibliothek Your knowledge hub WIEN

Chapter 2

Implementation

In this chapter, the implementation of the measuring system (according to Chapter 3) will be explained. Figure 2.1 depicts the overview of the whole system and the interactions between the elements. The displacement of the transducer is measured by the interferometer. The electrodes are used for generating a bias field the purpose of which is to mitigate electrostatic drift effects. Both the electrodes and the interferometer are connected to the main board where the interferometer signal is demodulated. In the case of the electrodes, the digital output is converted into an analog voltage value. The main board sends the measured data to the microcontroller unit (MCU) that is in charge of data modification like offset removal and averaging as well as actuating the electrodes. Lastly, the data is received by the Raspberry Pi (RPi) where it is stored, transformed into a frequency spectrum and visualized. Since this system is designed for mobile use, it is battery powered and the user can wirelessly connect with another (RPi) to operate the user interface.

Die approbierte gedruckte Originalversion dieser Diplomarbeit ist an der TU Wien Bibliothek verfügbar
The approved original version of this thesis is available in print at TU Wien Bibliothek.
TU WIEN Bibliothek Your knowledge hub

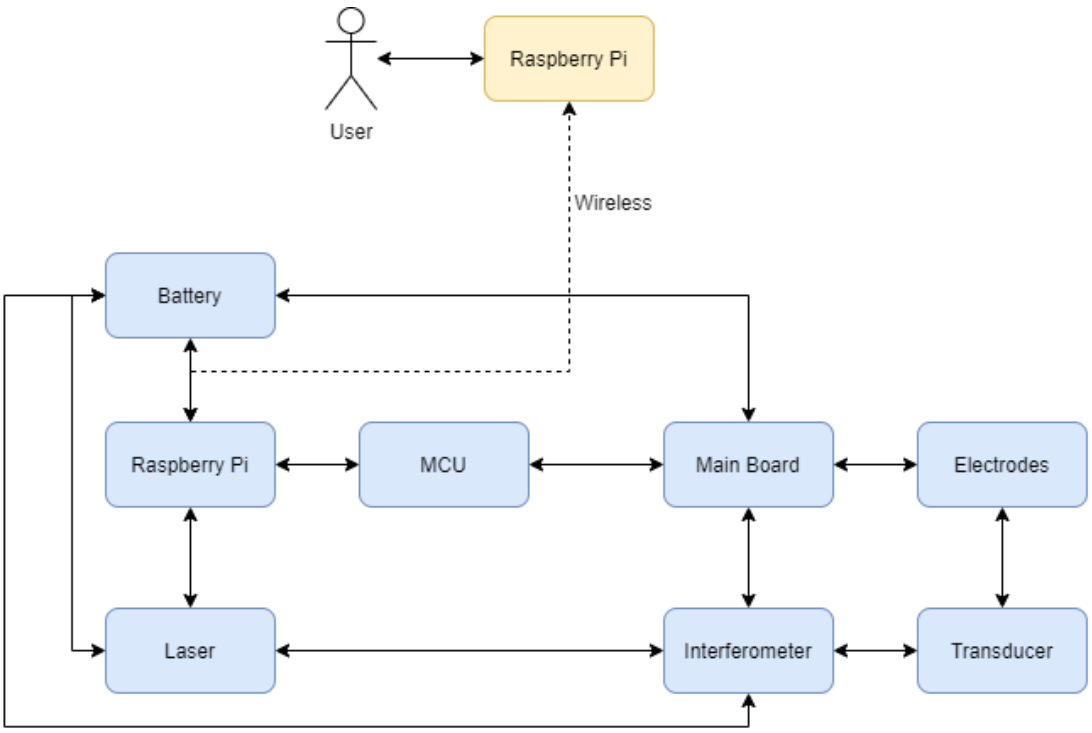

Figure 2.1: Block diagram of the components and their relations

2.1 MEMS Transducer

Several different transducer geometries were designed and tested so that the optimal shape and size could be established. The process of simulating and testing three different shapes, resembling the structure of the letters I, U and T is explained in [24] and it is analogous to the development of the cantilevers for this system. Additional to the shape, the U- and T-cantilevers were analyzed with and without combs on their cross-beams (Fig. 2.2). The combs serve the purpose of increasing the capacity of the cantilever, thus increasing the electrostatic force that acts upon the cantilever. For the results in Chapter 3, two different cantilevers were used. The first set of measurements was performed with the PI Controller explained in Section 2.2. The cantilever used for these measurements was a T-cantilever with combs. It was 2 mm long and the cross-beam was 1 mm long and 200 µm wide with a resonance frequency of 2.4 kHz. For the second set of measurements, the PI controller was not used. A constant voltage on the bias electrodes was applied instead. The cantilever used for these measurements was U-cantilever with combs on. It was 2 mm long and the cross-beam was 1 mm long and 100 µm wide with a resonance frequency of 3.96 kHz. The

Die approbierte gedruckte Originalversion dieser Diplomarbeit ist an der TU Wien Bibliothek verfügbar
The approved original version of this thesis is available in print at TU Wien Bibliothek.
TU Bibliothek Your knowledge hub WIEN

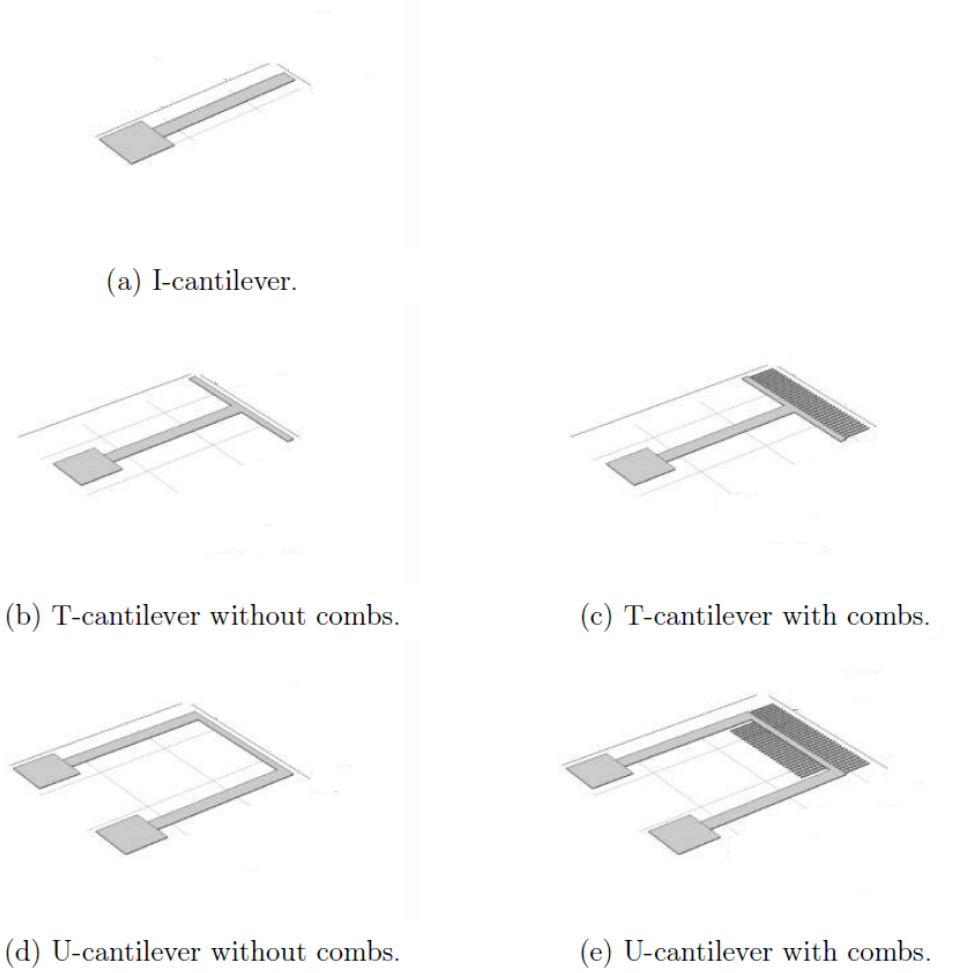

(a) I-cantilever.

(b) T-cantilever without combs.

(c) T-cantilever with combs.

(d) U-cantilever without combs.

(e) U-cantilever with combs.

Figure 2.2: I-,U- and T-cantilevers. The U- and T-cantilevers can be with and without combs on their cross-beam (modified from [24])

higher resonance frequency comes from the fact that the cross-beam was half as wide as the one of the T-cantilever, reducing the mass of the oscillator and thus increasing the resonance frequency according to the Eq. 1.26. Since the laser used for the optical readout had a wave length of 1300 nm at which the silicon has a relatively low reflectance (45 %), the cross-beam was covered with a 120 nm gold layer by evaporation deposition for higher reflectance and thus a better readout.

Die approbierte gedruckte Originalversion dieser Diplomarbeit ist an der TU Wien Bibliothek verfügbar
The approved original version of this thesis is available in print at TU Wien Bibliothek.
TU WIEN Bibliothek Your knowledge hub

2.2 PI Controller

As explained in Subsection 1.4.6, there is an observable drift in the measurements that can have many possible causes, but can be traced back to the dielectric materials in the proximity of the MEMS. One approach to mitigate this problem was to design a proportional–integral–derivative controller (PID controller) in a control loop that employs feedback through the bias electrodes back onto the MEMS, thus compensating for the drift. It is worth mentioning that the derivative component was 0, so the controller can be referred to as the PI controller.

To be able to design a controlling system, the MEMS itself had to be modelled first. The model was created in accordance with the observed behavior of the MEMS under different external field configurations and it is depicted in Fig. 2.3. It can be described as a negative feedback closed-loop system with a PI controller inside its open-loop transfer function (integrator Gain and MEMS Integrator from Fig. 2.3 are P and I components, respectively). As empirically observed, the MEMS had a certain setpoint at which it was operating even when the external field was not applied. Every time an external field was applied it would cause a jump in the MEMS output that would slowly dissipate back into the setpoint state due to the electrostatic drift. This means that for an external DC field, after the output value has dissipated back to the setpoint value, it was impossible to differentiate if the external field was on or off.

To solve this problem, a PI controller was implemented around the MEMS as depicted in Fig. 2.4. The input of the controller is the difference between the current MEMS output and the setpoint value, which the controller then tries to compensate by creating a new voltage for the bias electrodes as an output. The voltage on the bias electrodes is then added to the external field and their sum represents the new value of the electric field that is sensed by the MEMS.

This way, the actual measurement signal is not the MEMS output anymore, but the output of the PI controller, because it represents the strength of the field to be compensated. The implementation goal is to set the parameters of the controller in a way that it compensates the external field faster than the intrinsic compensation of the MEMS. The system was simulated with many different PI values that cause slower or faster compensation. An example of a fast compensation is depicted in Fig. 2.5. The yellow line represents an external field that was simulated as a rectangle signal. The green line represents the output of the MEMS before it reaches the PI controller (labeled Subsystem in Fig. 2.5). It can be observed how even in the absence of the electric field the MEMS output goes up to

Die approbierte gedruckte Originalversion dieser Diplomarbeit ist an der TU Wien Bibliothek verfügbar
The approved original version of this thesis is available in print at TU Wien Bibliothek.
TU Bibliothek Your knowledge hub WIEN

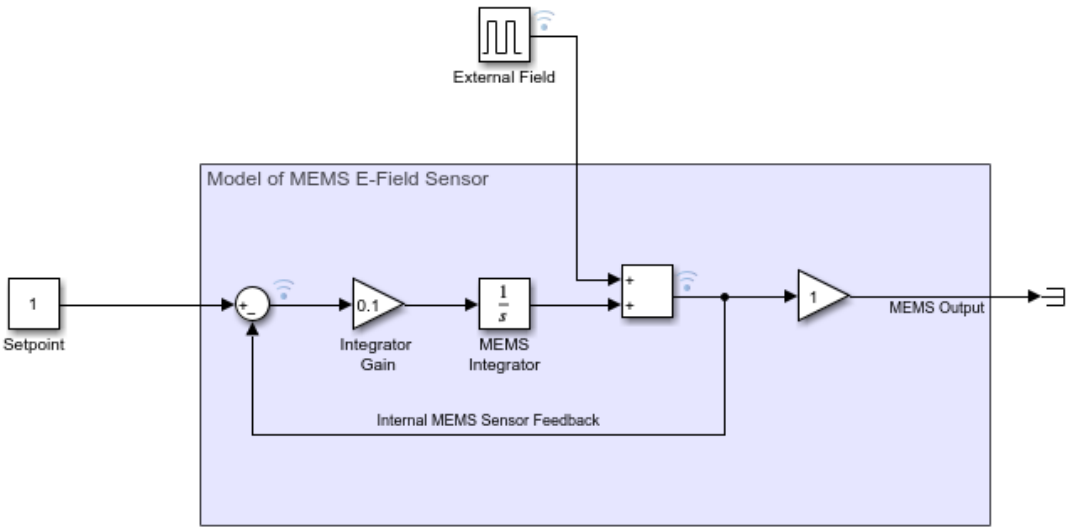

Figure 2.3: Model of the MEMS sensor with the observed drift behavior in a form of a negative feedback loop

a fixed setpoint, which corresponds with the observed behavior. The output of the PI controller is represented with a purple line and it mirrors the changes of the external field but with a inverted polarity since it is trying to compensate it. The simulation shows good responsiveness to the abrupt changes that the rectangle external field signal provides.

Die approbierte gedruckte Originalversion dieser Diplomarbeit ist an der TU Wien Bibliothek verfügbar
The approved original version of this thesis is available in print at TU Wien Bibliothek.
TU Bibliothek Your knowledge hub WIEN

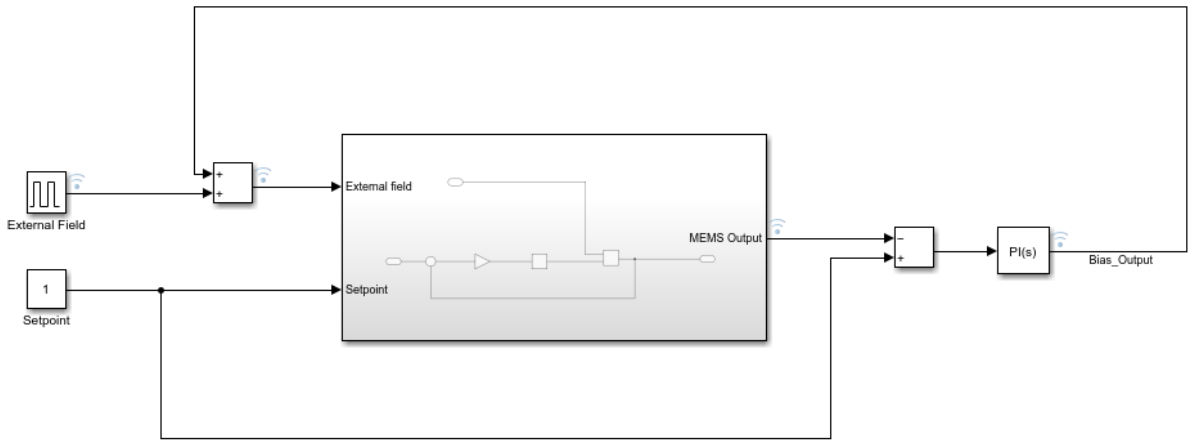

Figure 2.4: MEMS model with the PI controller

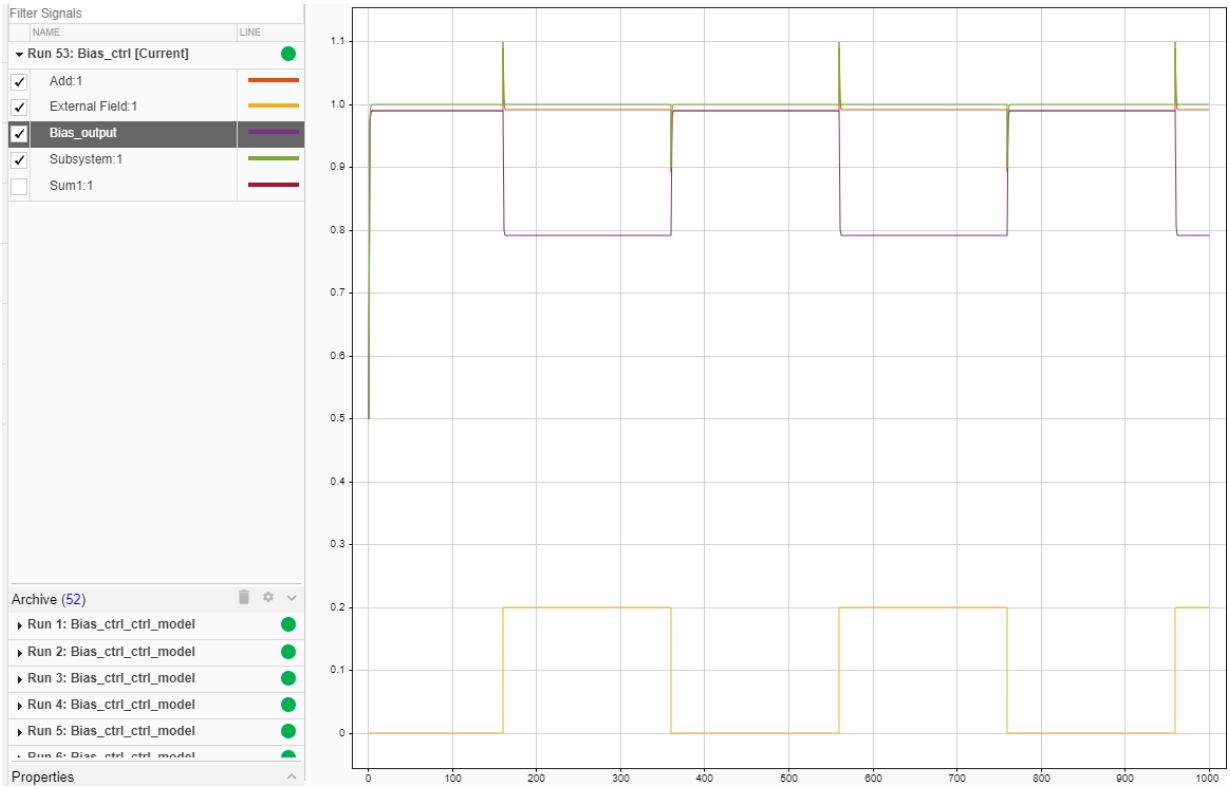

Figure 2.5: Simulation of the MEMS with the PI controller

Die approbierte gedruckte Originalversion dieser Diplomarbeit ist an der TU Wien Bibliothek verfügbar
The approved original version of this thesis is available in print at TU Wien Bibliothek.
TU WIEN Bibliothek Your knowledge hub

2.3 Main Board

The main board is in charge of demodulation of the interferometer signal and the controlling of the electrodes. The final version of the printed circuit board can be seen in Fig. 2.6.

2.3.1 Demodulation

When the interferometer signal first enters the board it is filtered through a high pass filter with a cut-off frequency of 700 Hz. Since the signal is modulated at approximately 3.9 kHz, this trims down the spectrum to avoid overlapping of spectra when the signal is demodulated back to 0 Hz (analogous to modulation in Fig. 1.11). Another reason for the high pass filter is the filtering of the unmodulated squared component of the electric field (first term in Eq. 1.34). Afterwards, the signal is amplified through a preamplifier with a gain ratio of 10 (3.1 dB). The amplification is done in the early phase of the signal processing on the board to minimize the noise of other components on the sensor signal. The signal is then demodulated using the I/Q (in-phase and quadrature) demodulation. This demodulation algorithm divides the signal into two components that are phase-shifted by 90°, which creates a complex signal vector that contains the amplitude and the phase of the modulated signal. In the case of simple demodulation, only a real component of the signal would be available, so each phase shift would lower the amplitude value resulting in measurement error. The phase also holds the information of the polarity of the amplitude.

The diagram of the demodulation is depicted in Fig. 2.7. The interferometer is driven at the resonance frequency f_{drive} by the DDS (direct digital synthesis) frequency generator. The interferometer signal is firstly divided into two components, one of which is inverted. Each component is then multiplied with a rectangle signal that is achieved by two switches that are driven at the resonance frequency but with a 90° phase shift between them. This is achieved with a DDS (direct digital synthesis) frequency generator at a frequency two times the resonance frequency $2f_{\text{drive}}$. The generator signal is then divided in two branches, one is inverted and then frequency of both branches is multiplied by one half so that the pulses are at the resonance frequency. At this point, the signal is already demodulated because it has been multiplied with the resonance frequency at which it was originally modulated (Eq. 1.34) and divided into in-phase and quadrature (I/Q) components. Lastly, the two components are filtered through the 3rd order low pass filter with a cut-off frequency of 1 kHz. This is the cut-off frequency explained in Subsection 1.4.6.

Die approbierte gedruckte Originalversion dieser Diplomarbeit ist an der TU Wien Bibliothek verfügbar
The approved original version of this thesis is available in print at TU Wien Bibliothek.
TU Bibliothek Your knowledge hub WIEN

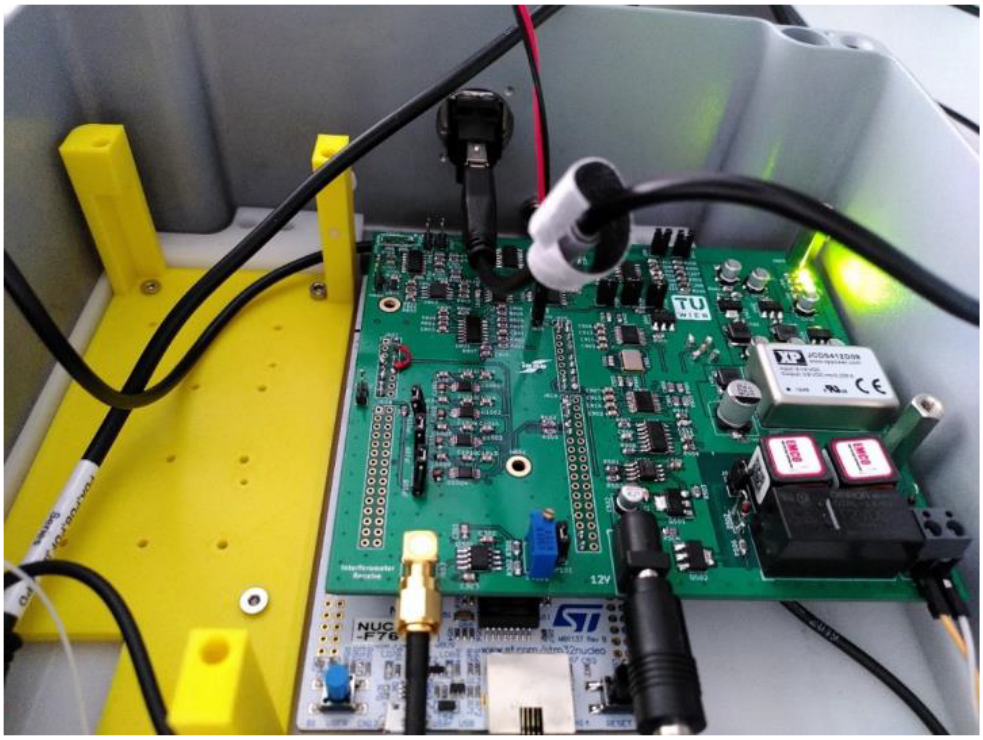

Figure 2.6: Photo of the main board used for demodulation and controlling of the electrodes. The microcontroller is visible underneath the board

2.3.2 ADC

After the demodulation, the analog I/Q signals are ready for conversion into digital signals so that they can be further processed by the microcontroller. The most important parameter of the analog-digital-converter (ADC) is the sampling rate. According to Nyquist's Theorem, the sampling rate has to be at least two times higher than the highest frequency in the signal to be sampled. This is again related to the frequency spectrum overlap explained in Subsection 1.4.6. The difference is that the signal is not multiplied with a sine wave that corresponds to two Dirac impulses symmetrical about the y-axis, but with a signal that has a comb shaped frequency spectrum (many Dirac impulses). The principle is the same in a sense that low sampling rate corresponds to the tighter impulses in the frequency spectrum, which leads to an overlapping of the mirrored signals. Since the cut-off frequency used was 1 kHz, that is also the highest frequency component of the signal. The double sampling rate is the minimal condition for the signal reproduction in digital form but a much higher sampling rate is always desirable. Also, the advantage of analog demodulation is that the demodulated signal has significantly lower frequency and thus can be sampled

Die approbierte gedruckte Originalversion dieser Diplomarbeit ist an der TU Wien Bibliothek verfügbar
The approved original version of this thesis is available in print at TU Wien Bibliothek.
TU Bibliothek Your knowledge hub WIEN

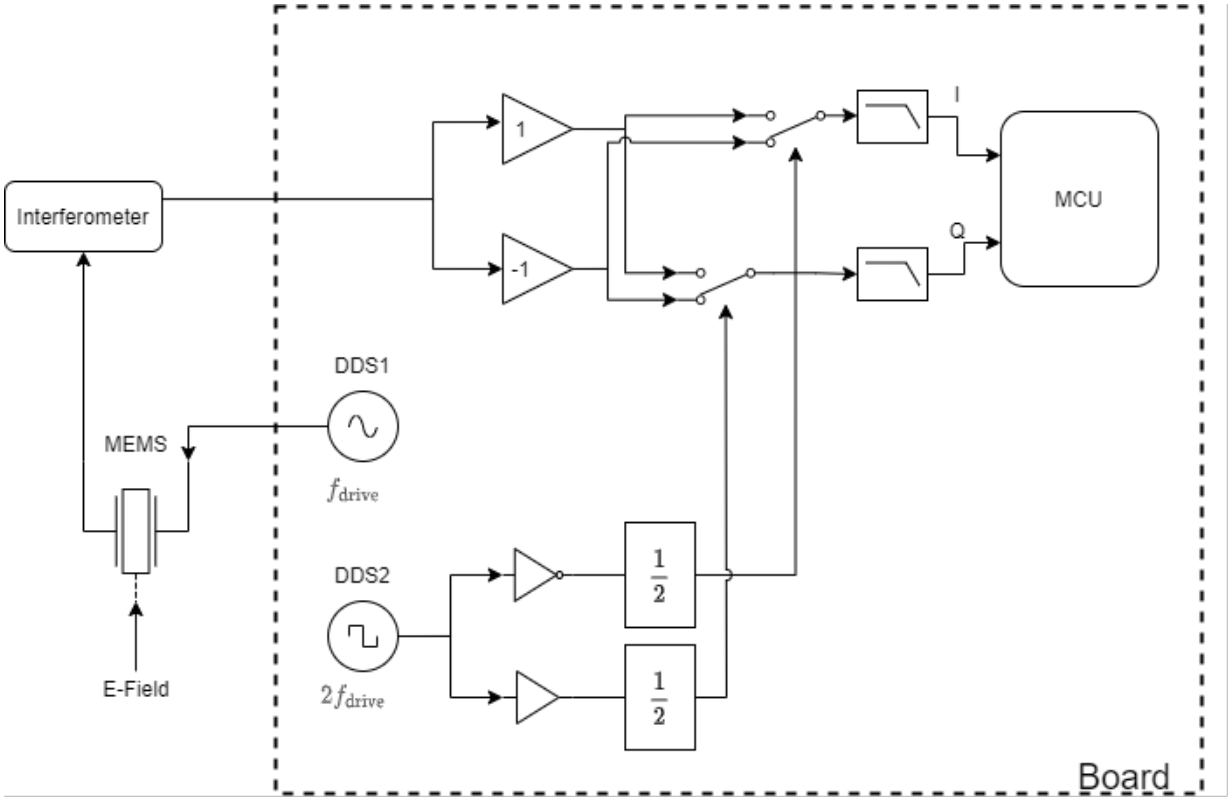

Figure 2.7: Diagram of the demodulation component of the main board

at a much lower sampling rate. Taking all these factors into consideration, a sampling rate of 10 $\frac{\text{kSamples}}{\text{s}}$ was chosen.

The ADCs used can only output positive values in a form of an unsigned 16-bit integer. For the full ADC output range of 2^{16} values and for both positive and negative values, an offset to the middle of this range was used. This way the signed range can be interpreted as $\pm 2^{15}$.

2.3.3 Bias Electrodes Control

The electrodes are controlled by the microcontroller where the digital value sent by the MCU is converted on the main board into an analog signal using a digital-analog-converter (DAC). The output voltage range of ±250 V is achieved with two high voltage sources (Fig. 2.8) that are supplied with a 12 V input that is then transformed to 250 V. On the right side of the circuit diagram is the current mirror that mirrors the current from the 3.3 V on the left side onto the right side where the voltage is 250 V. From the two branches, only one is active at a time while the other one is blocked by the transistors, allowing one

Die approbierte gedruckte Originalversion dieser Diplomarbeit ist an der TU Wien Bibliothek verfügbar
The approved original version of this thesis is available in print at TU Wien Bibliothek.
TU Bibliothek Your knowledge hub WIEN

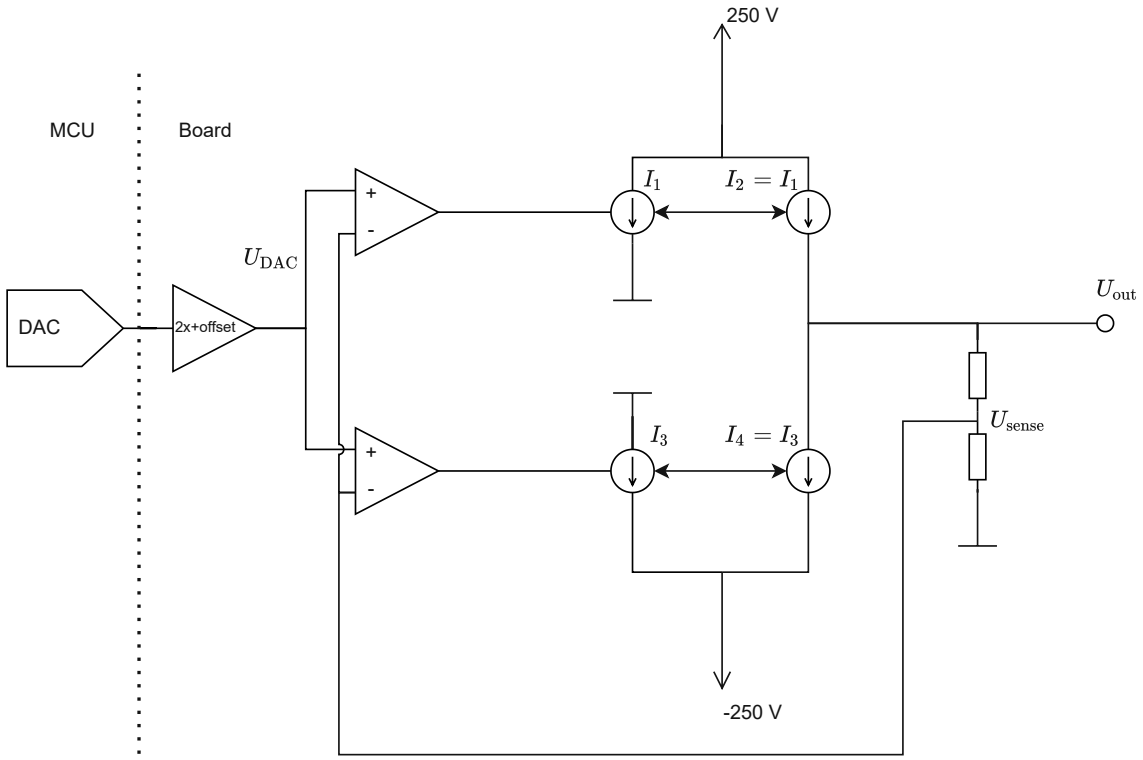

Figure 2.8: Diagram of the bias electrodes controlling circuit

branch to work for the positive and the other for the negative voltage values. Lastly the two op-amps on the mentioned branches are connected with the voltage divider on the right side of the mirror. The divider creates the relation between the ±3.3 V input and the ±250 V output that controls the electrodes.

2.4 Microcontroller

For this project a microcontroller unit from the family of STM32 was chosen. Their widespread use lead to the development of various integrated development environments (IDE) and useful driver libraries which all make the development process easier. The microcontroller used for this system is a "Nucleo"-evaluation board STM32F767ZI. The evaluation boards have all of the interfaces and already setup, which allows for faster prototyping and easier connectivity to external components. The main board was mounted on top of the STM, so that the pins for the ADCs and other controlling signals can be directly connected (Fig. 2.6). The communication with the Raspberry Pi computer was achieved using an UART interface that is explained in 2.5.2.

Die approbierte gedruckte Originalversion dieser Diplomarbeit ist an der TU Wien Bibliothek verfügbar
The approved original version of this thesis is available in print at TU Wien Bibliothek.
TU WIEN Bibliothek Your knowledge hub

The microcontroller software architecture is designed as a finite state machine (FSM). An FSM is a mathematical model that describes a system that has a finite number of states that it can be in. Furthermore, the system has a finite number of expected inputs that can lead to clearly defined outputs as well as state transitions. A software designed in this form has an advantage of being predictable and less prone to unexpected errors if designed properly. The disadvantage is its low scalability, but since the goal of the MCU in this system is relatively simple, this wasn't an issue. The microcontroller starts in an idle state, where it awaits an input command. Depending on the input, it enters one of the co-routines, some of which will be explained in the following subsections. During the co-routine execution, the system can be brought back into an idle state with a stop command.

2.4.1 PI Controller Co-Routine

As explained in Section 2.2, the PI control loop was implemented to compensate the drift by controlling the voltage on the bias electrodes. The diagram of the data processing path is depicted in Fig. 2.9 and since the majority of the processing steps are similar to other co-routines, it gives a good overview of the overall functionality of the microcontroller.

Firstly, the digital data converted on the main board is read onto the microcontroller. Since the I/Q values contain the ADC offset explained in 2.3.2, the offset is subtracted from the I and Q values. They are used to calculate the magnitude and the phase of the current vector. In the next step a moving average is applied onto the values for the last 100 data points. After the magnitude information is extracted from the data, the phase information is only needed for the polarity of the magnitude, so it is used used in sign function $\mathrm{sgn}(x)$ and multiplied with the magnitude. Finally the magnitude with the correct polarity is passed onto the PID controller that calculates the new voltage for the bias electrodes that is then transformed into an analog value and sent back to the main board. This co-routine repeats this process indefinitely long i.e. until it is halted by the user.

2.4.2 Setpoint Co-Routine

As mentioned in Section 2.2, the MEMS showed a certain offset from the zero value output even when no electric field was applied. This setpoint was slightly different depending on the environment conditions and it was needed to establish the setpoint every time before the measurements were carried out. To establish the setpoint, the system is activated without the PI stabilization and shielded from the outer electric fields. The measurement

Die approbierte gedruckte Originalversion dieser Diplomarbeit ist an der TU Wien Bibliothek verfügbar
The approved original version of this thesis is available in print at TU Wien Bibliothek.
TU WIEN Bibliothek Your knowledge hub

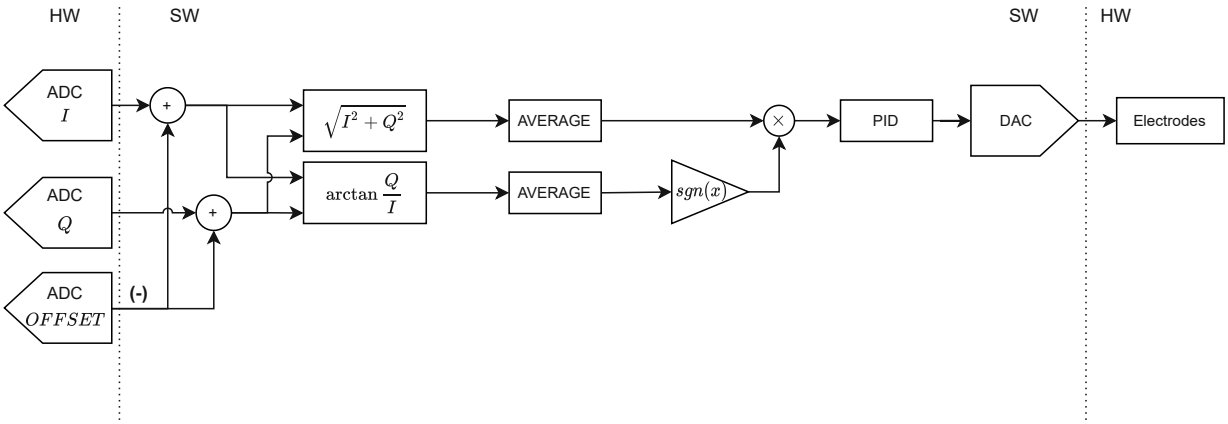

Figure 2.9: Diagram of the microcontroller data processing path for the PI co-routine

was then performed for a fixed time period (e.g. 30 seconds) and the mean value of the amplitude with the corresponding polarity that is acquired from the phase was used as the setpoint for the rest of the active measuring session.

2.4.3 Round-trip Co-Routine

For the analysis and testing purposes, another co-routine was developed that gave insight into the response of the system on a dynamical change of the electric field, as well as investigate potential short term drift, hysteresis and saturation in the measuring domain. Namely, the bias control voltage was redirected to generate a test field by connecting it to a metal plate parallel to the MEMS. The advantage of this test method is that the bias voltage can be easily controlled by the microcontroller and the values used for the test can be easily stored together with the data measured as the reaction to their field synchronously. The co-routine changed the voltage in incremental steps from 0 V to 250 V, which is the maximal possible output voltage, then all the way down to the minimal possible voltage of −250 V before returning incrementally back to 0 V. This way the measured values for the same electric field can be compared between the upward and downward "path" of the electric field. In the case of a drift, the two values would be different and a hysteresis would be observed. Also the saturation in the range of high values would be observed in a form of deviation from the linear dependency between the applied voltage and the measured signal.

Die approbierte gedruckte Originalversion dieser Diplomarbeit ist an der TU Wien Bibliothek verfügbar
The approved original version of this thesis is available in print at TU Wien Bibliothek.
TU Bibliothek Your knowledge hub WIEN

2.5 Graphical User Interface Software

The graphical user interface (GUI) software allows the interaction of a user with the sensor. The user is able to control the sensor as well as see the measurement results in real time.

2.5.1 Operating System and GUI Framework

The GUI developed for this sensor was written in Python (v3.9) using the PySide2 module, that is a Python implementation of the Qt Framework that is originally developed for the C++ programming language. This module was chosen over the PyQt5 module that offers an almost identical functionality because of licensing differences. PySide2 is published under the LGPL (GNU Lesser General Public License) that leaves more freedom for commercial use than its rival PyQt5 with the GPL v3 License (GNU General Public License v3.0). The software is running on a Raspberry Pi 4 with Raspberry Pi OS (operating system) that is a Linux distribution officially developed by the RPi foundation. Additionally Manjaro and Ubuntu were tested as OS alternatives but Manjaro was ruled out because of its inferior software support and Ubuntu was resource intensive, so RPi OS remained the best choice.

2.5.2 UART Communication

Since the communication between the microcontroller and the RPi was done using an UART Interface, it was critical that the data was accessed by the RPi fast enough to avoid a buffer overflow. The RPi is not a real-time OS, so the thread responsible for the readout of the UART data could potentially lose its priority in the kernel and read the data too late. This problem was solved with careful parametrization of the UART interface as well as the reading thread. The 6-byte data-word consists of three 16-bit integers that represent the I, Q and the PID values. The data-word is read in the blocks of 100 words in a dynamic array so that the UART physical buffer is not overwritten. This process is repeated 100 times before the data is written from the dynamic memory to a file. This hierarchical pipeline between the readout and the save process adequately solves the trade-off between the number of save operations that are resource intensive and slow and the readiness of the new data to be represented in the live plot. Since the data is sent with a 10000 $\frac{\text{Samples}}{\text{s}}$ and between the reading and writing there are two buffers of size 100 ($100 * 100 = 10000$), the live plot is updated every second. The data has to be further analyzed before the plotting but that is done in another thread to free up the reading thread since it is time-critical.

Die approbierte gedruckte Originalversion dieser Diplomarbeit ist an der TU Wien Bibliothek verfügbar
The approved original version of this thesis is available in print at TU Wien Bibliothek.
TU Bibliothek Your knowledge hub WIEN

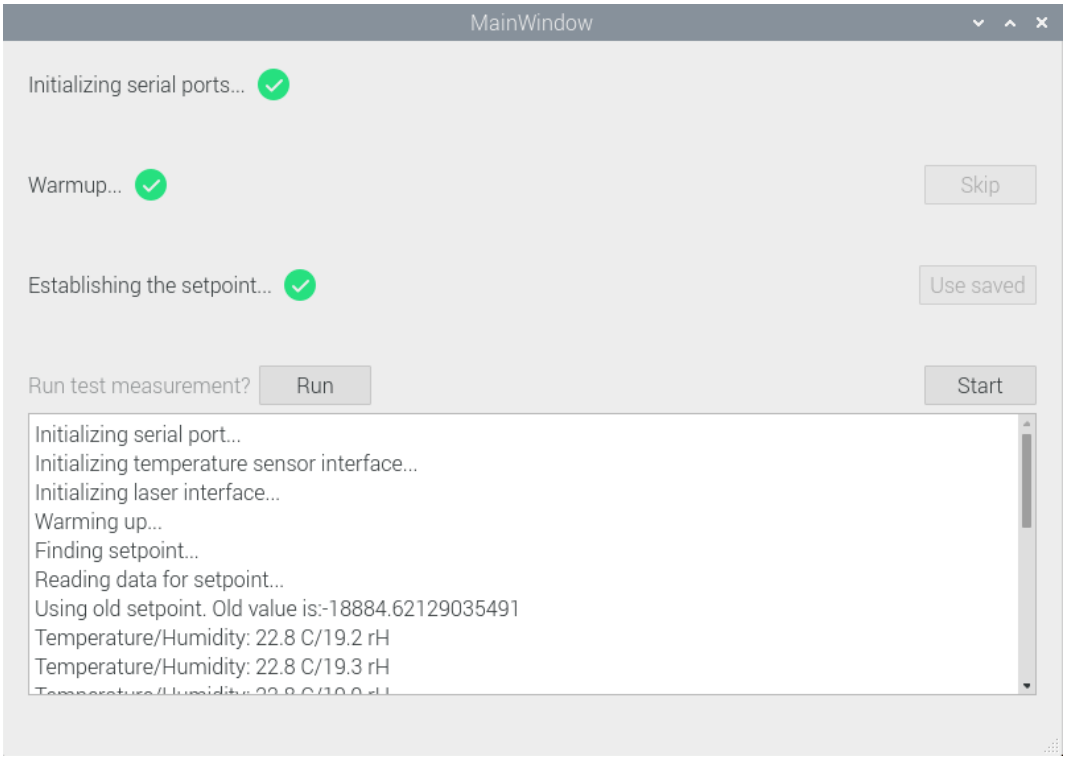

Figure 2.10: Initialization window of the sensor software

2.5.3 Initialization and Warmup

When the program is started and after the password is entered correctly on the start window, the initialization process is triggered and the initialization window is displayed (Fig. 2.10). Firstly, the interfaces with the microcontroller, the temperature sensor and the interferometer are initialized. If the initialization was successful, the system enters a warmup phase where the system is idle for 30 seconds and the user is informed about the temperature and the humidity during this time. Afterwards the setpoint is established as explained in 2.4.2 or the last saved setpoint value can be chosen. In the last step of this phase, a test measurement can be optionally performed, which activates the round-trip co-routine explained in 2.4.3.

2.5.4 Main Window

If the initialization was successful, the main window of the program is opened (Fig 2.11). The most of the window's surface is covered with the frequency spectrum graph of the live measurement that is updated each second with the data received from the microcontroller.

Die approbierte gedruckte Originalversion dieser Diplomarbeit ist an der TU Wien Bibliothek verfügbar
The approved original version of this thesis is available in print at TU Wien Bibliothek.
TU Bibliothek Your knowledge hub WIEN

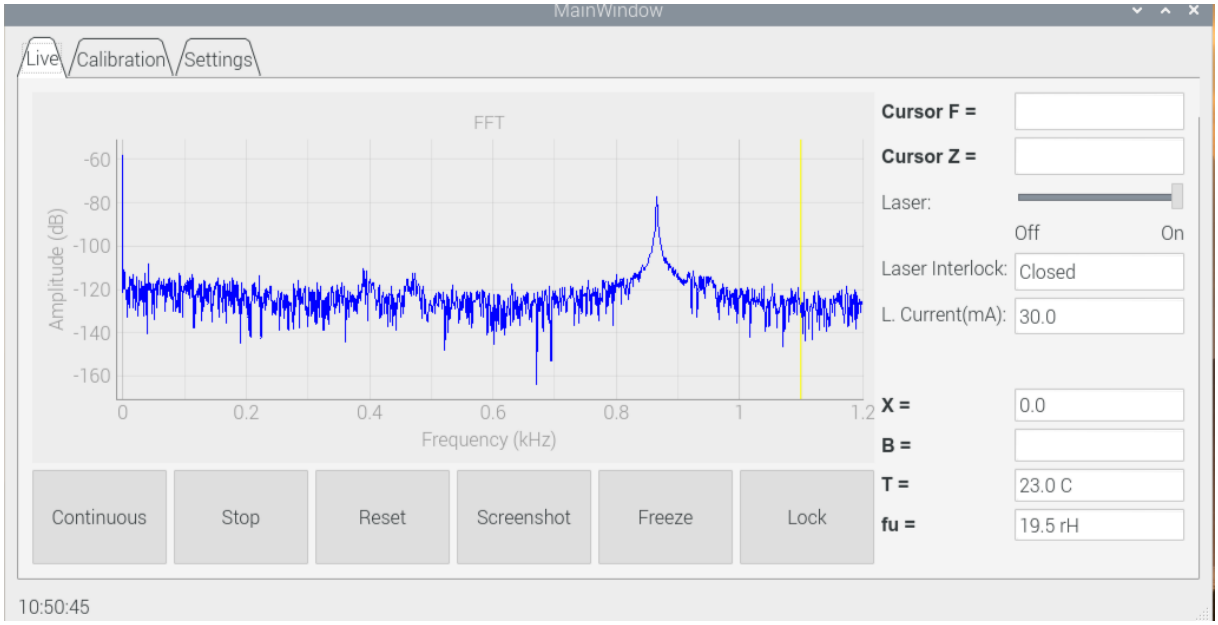

Figure 2.11: Main window of the sensor software

The I and Q component that are received are used to calculate the magnitude of their vector, which is then passed onto the FFT (fast Fourier transformation) function for the frequency spectrum calculation. This process is triggered every second in a background thread that sends a signal to the main thread every time the calculations are done and the data is ready for plotting. The resolution of the graph depends on the number of data points used for the FFT transformation and this can be set in the settings tab of the window. Even though the sampling rate is 10000 $\frac{\text{Samples}}{\text{s}}$ and thus the FFT delivers the spectrum range of 5 kHz (Nyquist's theorem), the measurements for higher frequencies are less important and prone to interference, so a yellow vertical line indicates that the values over 1.1 kHz should not be considered.

Die approbierte gedruckte Originalversion dieser Diplomarbeit ist an der TU Wien Bibliothek verfügbar
The approved original version of this thesis is available in print at TU Wien Bibliothek.
TU Bibliothek Your knowledge hub WIEN

Die approbierte gedruckte Originalversion dieser Diplomarbeit ist an der TU Wien Bibliothek verfügbar
The approved original version of this thesis is available in print at TU Wien Bibliothek.

Chapter 3

Results

In this chapter, the measurement results of two different system configurations are reported. The main difference in the configurations is the voltage on the bias electrodes. In the first configuration, the electrodes were controlled using the PI controller explained in Section 2.2 and in the second configuration, a constant voltage applied was applied on the bias electrodes. It is worth mentioning that the first configuration used a prism above the transducer to guide the laser beam onto the cantilever, whereas the prism was not used because of its dielectric interference with the measurements. Instead, all optical components were shielded inside the sensor housing.

3.1 Drift

One of the biggest challenges for reliable measurements was the electrostatic drift that was observed during measurements. The results in Fig. 3.1 show the drift of the measured voltage after an external field was applied. The external field was produced by applying a 100 V voltage on a plate above the sensor at a distance of 20 mm, which corresponds to an electric field intensity of $5\,\frac{\mathrm{kV}}{\mathrm{m}}$. After the electric field was applied, an amplitude slowly stabilized back onto the setpoint value, even though the field was still there. When the field was turned off, a similar jump in the amplitude can be observed followed by the stabilization back onto the setpoint. In this measurement, the MEMS was bonded into a ceramics package with the prism glued on top. This was held by a 3D-printed plastic mounting. The materials used here turned out to contribute to the electrostatic drift.

In order to better understand the cause of this drift, different materials were tested as the substrate material for the transducer. First, a conventional printed circuit board (PCB) material FR4, then the alumina ceramics (Al_2O_3) substrate and lastly a steel holder was

Die approbierte gedruckte Originalversion dieser Diplomarbeit ist an der TU Wien Bibliothek verfügbar
The approved original version of this thesis is available in print at TU Wien Bibliothek.
TU WIEN Bibliothek Your knowledge hub

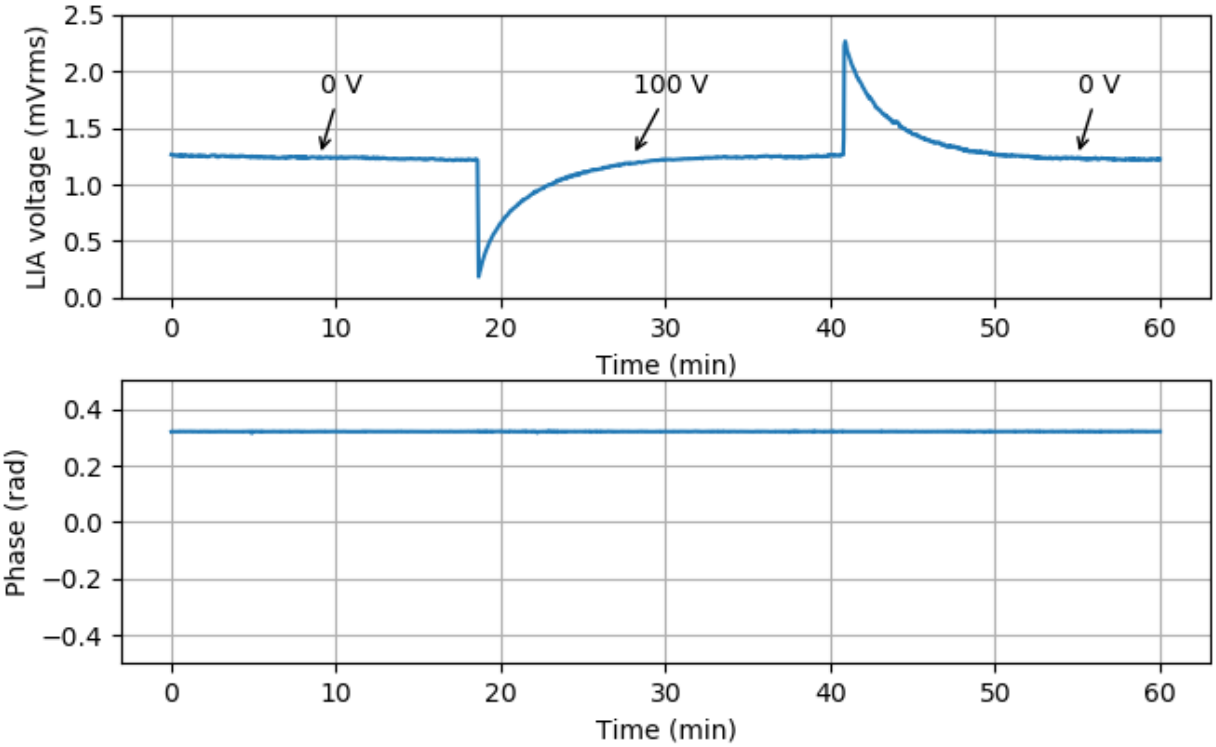

Figure 3.1: System stability under the influence of an external field. The interferometer voltage is represented in root mean square (RMS) values

used for the investigation of mechanical characteristics of the transducer. The measurements were conducted with no external field applied and the results are depicted in Fig. 3.2. Even though steel alone is not a valid option for the MEMS substrate, it was a good indicator that the drift was induced by a dielectric material, since no drift could be observed with the steel holder as any polarization process happens instantly in a metal. In the case of the ceramic substrate, the amplitude drifts until it reaches the balanced state after 4 hours, whereas the PCB substrate seems influence the amplitude constantly and a stable state could not be reached.

Die approbierte gedruckte Originalversion dieser Diplomarbeit ist an der TU Wien Bibliothek verfügbar
The approved original version of this thesis is available in print at TU Wien Bibliothek.
TU Bibliothek Your knowledge hub WIEN

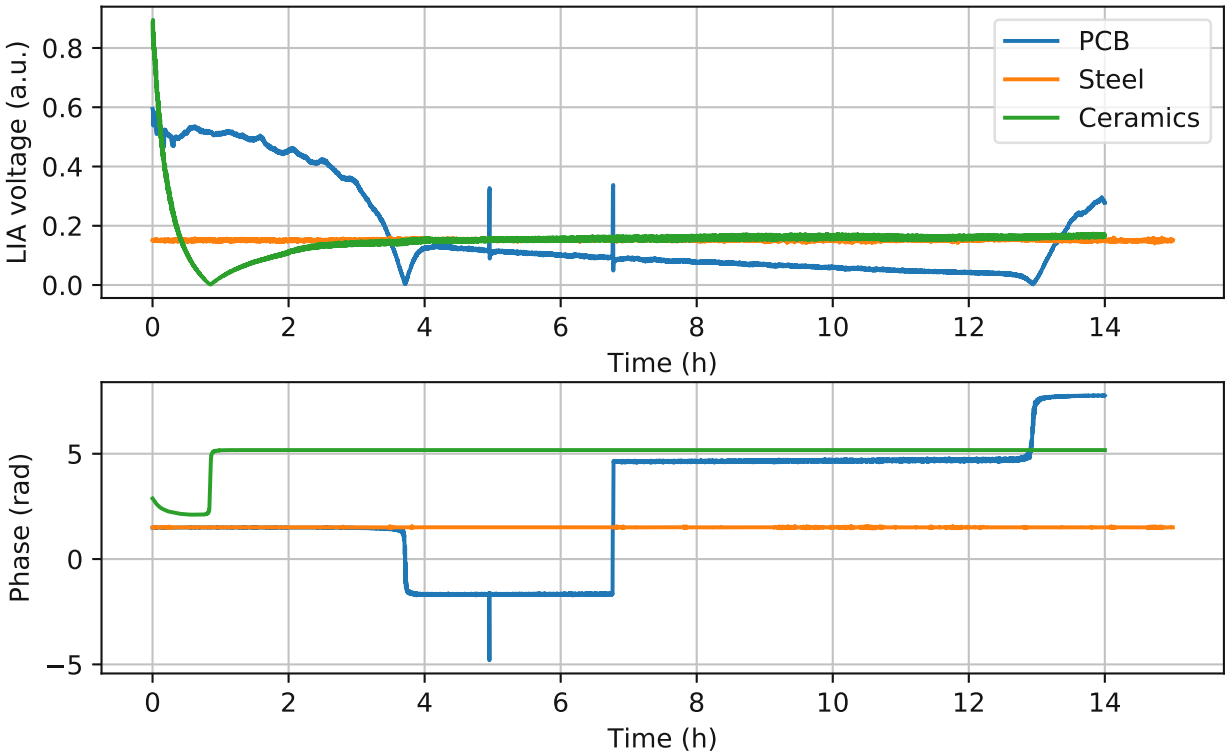

Figure 3.2: Comparison of different transducer substrate materials. No external field was applied

3.2 PI Measurements

To mitigate the drift observed in Section 3.1, a PI controller was implemented. The design started with a PID controller, but the simulations from Section 2.2 showed that the derivative component was not useful for the stabilization. This is why in some graphs the controller is still referred to as a PID controller. Early measurements with the PI controller are depicted in Fig. 3.3 for different P and I parameters. Depending on the parameters, the controller can be observed compensating the external field (100 V jump) slower or faster. Even though the amplitude stabilizes after approximately 2 minutes, the bias voltage (i.e the PI controller output) keeps increasing. Since in this configuration, the bias voltage should be interpreted as the actual measured value of the DC E-field, this represented a big problem. A possible reason is small changes in the setpoint of the transducer, towards which the controller tries to stabilize. When the actual setpoint differs from the one that was specified, the controller constantly tries to compensate that difference.

After further adjustments to the system (different pre-amplifier, new PI values) new measurements were conducted. The test setup consisted of a parallel plate capacitor with a

Die approbierte gedruckte Originalversion dieser Diplomarbeit ist an der TU Wien Bibliothek verfügbar
The approved original version of this thesis is available in print at TU Wien Bibliothek.
TU Bibliothek Your knowledge hub WIEN

plate size of $1\,\mathrm{m} \times 1\,\mathrm{m}$ and a plate distance of $50\,\mathrm{cm}$. The electric field that could be created inside the capacitor had a range of $\pm 20\,\frac{\mathrm{kV}}{\mathrm{m}}$. All the measurements had the same sequence: 30 seconds without any field, 3.5 minutes with the applied field and lastly 1 minute without any field. The results are depicted in Fig. 3.4 and are represented through the voltage applied onto the bias electrodes, since in this configuration, the bias voltage represents the measured value and not the interferometer amplitude. It can be observed that the control loop reacts faster and thus the responsiveness of the system on the abrupt field change is much faster. The issue of the setpoint variation and constant increase in the bias voltage persisted. Furthermore, the initial setpoint values of each measurement were different. This indicates that the bias field was not able to fully compensate the electrostatic drift in the dielectrics or that an additional mechanism takes place.

Therefore, it was concluded that the configuration with the prism on top of the MEMS was not beneficial and that as little dielectrics as possible should be near the MEMS. The measurement system was rebuilt with all optical components shielded inside the housing of the system. The MEMS itself was on the surface of the housing, where it was exposed to the external field and the displacement was measured by the interferometer from the inside. It turned out that this solved the problem of the electrostatic drift and that there was no need for the stabilization mechanism anymore.

Die approbierte gedruckte Originalversion dieser Diplomarbeit ist an der TU Wien Bibliothek verfügbar
The approved original version of this thesis is available in print at TU Wien Bibliothek.
TU Bibliothek Your knowledge hub WIEN

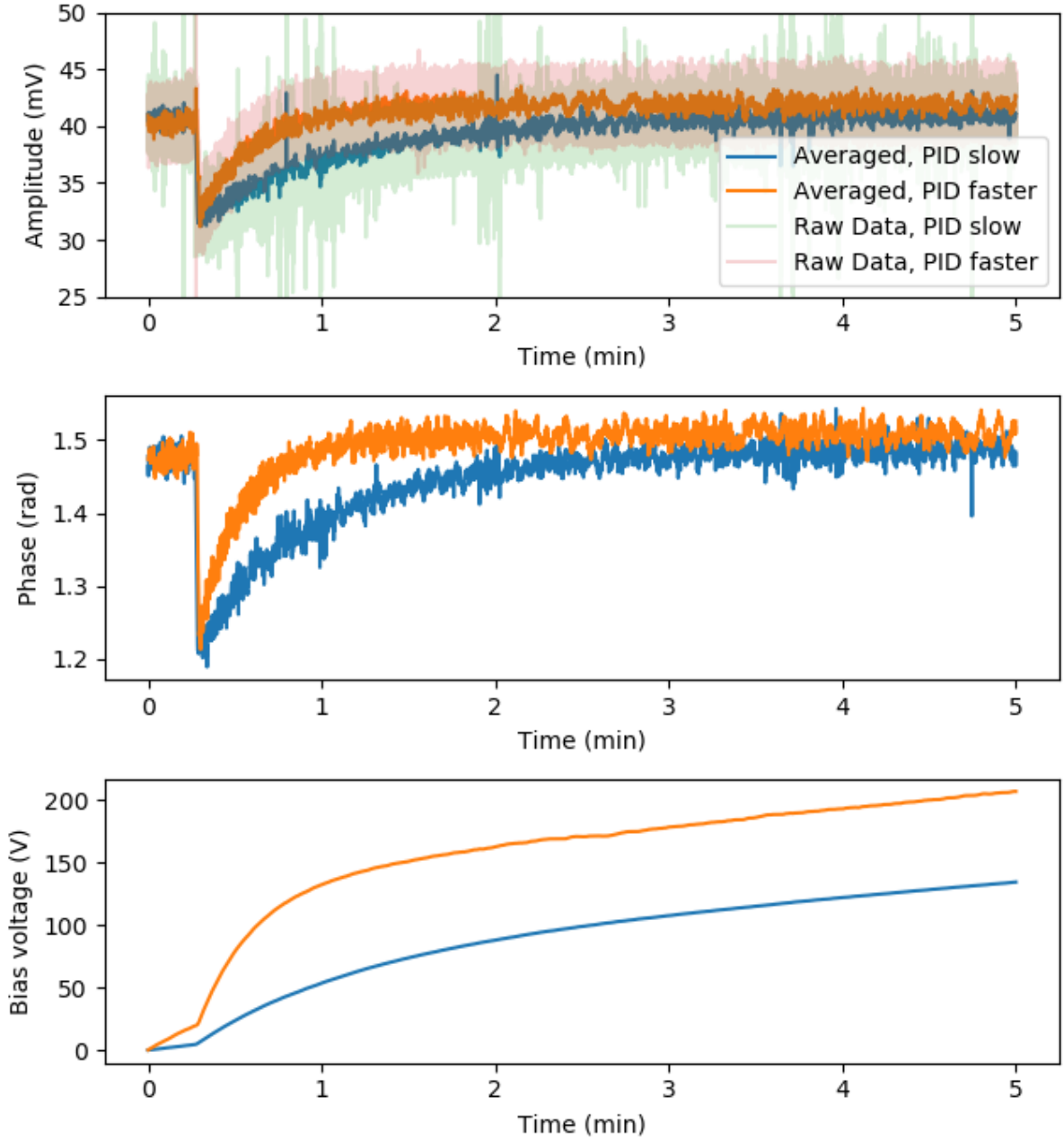

Figure 3.3: System response to a 100 V step. The amplitude stabilizes but the bias voltage keeps increasing

Die approbierte gedruckte Originalversion dieser Diplomarbeit ist an der TU Wien Bibliothek verfügbar
The approved original version of this thesis is available in print at TU Wien Bibliothek.

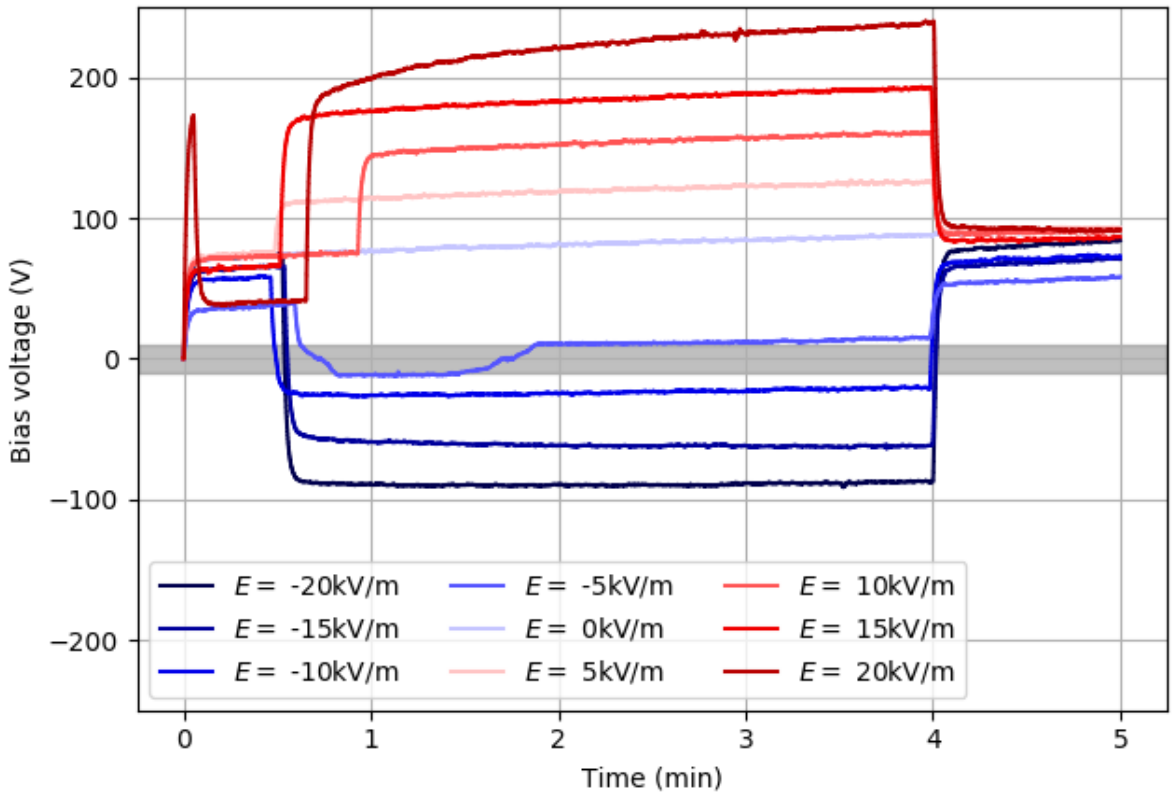

Figure 3.4: Measurement results for different electric field values in a $\pm 20\,\frac{\mathrm{kV}}{\mathrm{m}}$ range with the PI controller. Early jump in the $20\,\frac{\mathrm{kV}}{\mathrm{m}}$ curve is an accidental early power-on of the field

Die approbierte gedruckte Originalversion dieser Diplomarbeit ist an der TU Wien Bibliothek verfügbar
The approved original version of this thesis is available in print at TU Wien Bibliothek.

3.3 Constant Bias Measurements

Since the new configuration without the prism wasn't affected by the electrostatic drift, there was no need for the PI control mechanism anymore. On the other hand, the ions could still effect the measurement results, which is especially concerning in ionic environments such as below HVDC transmission lines. This effect can be mitigated by applying a fixed voltage on the bias electrodes. The ions are then, depending on their polarity, either get deflected by the electrodes or be attracted by them. The measurement value now is not the bias output voltage, but the actual measured amplitude, however with an offset stemming from the constant bias voltage that was applied.

The measurement depicted in Fig 3.5 is conducted using the round-trip co-routine explained in Section 2.4.3 but the bias voltage output was applied to an external plate instead of the bias electrodes, which were driven at a constant voltage of 100 V. The plate was at a distance of 3.5 cm from the transducer, which means that the voltage range of ±250 V produced an electric field range of $\pm 7.14\,\frac{\mathrm{kV}}{\mathrm{m}}$. The measurements showed much better results than with the previous configuration. The system was highly responsive to the incremental changes of the electric field, while maintaining a linear correlation between the external field and the measured voltage, which can be seen when compared to the linear fit function extracted from the data. Also there is no hysteresis in the measurements which implies that the system is not experiencing drift anymore.

These measurements were conducted for multiple constant bias voltages ranging from −200 V to 200 V, that are depicted in Fig 3.6. It can be observed that the linear dependability remains preserved for all tested bias voltages, as well as the negative slope of approximately −0.05 mV/V or in the terms of the electric field applied $-1.7\,\mathrm{mV}/\frac{\mathrm{V}}{\mathrm{m}}$.

Die approbierte gedruckte Originalversion dieser Diplomarbeit ist an der TU Wien Bibliothek verfügbar
The approved original version of this thesis is available in print at TU Wien Bibliothek.
TU WIEN Bibliothek Your knowledge hub

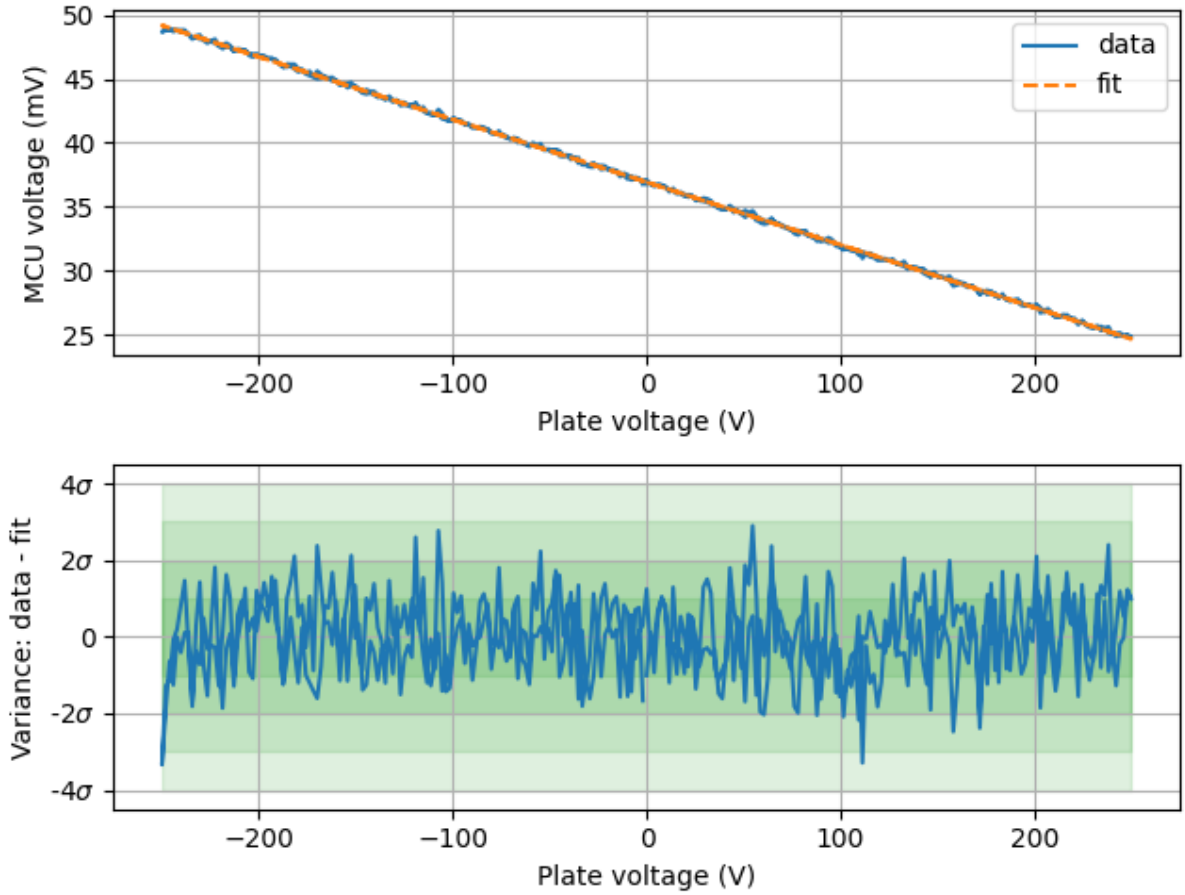

Figure 3.5: Round-trip measurements for a 100V bias voltage. The plate was at a distance of 35 cm

Die approbierte gedruckte Originalversion dieser Diplomarbeit ist an der TU Wien Bibliothek verfügbar
The approved original version of this thesis is available in print at TU Wien Bibliothek.

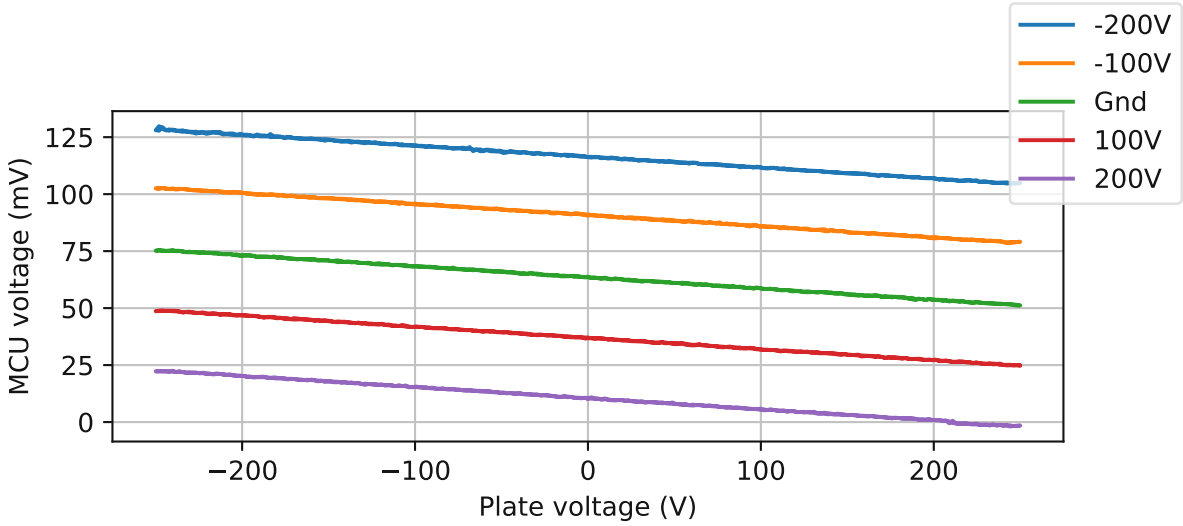

Figure 3.6: Round-trip measurements for different bias voltages

Die approbierte gedruckte Originalversion dieser Diplomarbeit ist an der TU Wien Bibliothek verfügbar
The approved original version of this thesis is available in print at TU Wien Bibliothek.

Die approbierte gedruckte Originalversion dieser Diplomarbeit ist an der TU Wien Bibliothek verfügbar
The approved original version of this thesis is available in print at TU Wien Bibliothek.

Conclusion and Outlook

Conclusion

The first part of this thesis covered the fundamentals needed to understand the working principle of the micro-electromechanical systems. Both electrostatic as well as mechanical mechanism applied in the MEMS sensors are explained. The research and development of a new sensor design was also motivated by discussing the state-of-the-art electric field sensors and their flaws, especially when it comes to the DC field measurements. Further important aspects of an active field sensor such as the signal modulation and the recovery of the measured spectrum as well as the challenge of an non intrusive optical readout are also discussed. The biggest challenge of the DC field measurements - the electrostatic drift - was covered, as well as the possible causes of this unwanted phenomenon.

The second chapter goes over the implementation of the sensor used for the provided measurements. Apart from the MEMS design, the challenges of fast data acquisition and demodulation, as well as signal processing on a custom designed printed circuit board were explained. Additional to the hardware signal processing, the software signal processing that took place on a microcontroller was also mentioned. The microcontroller was also in charge of the control loop mechanism implemented to mitigate the electrostatic drift effects. Lastly, the end-user software that was used for the data acquisition, management and visualization was explained.

The measurement results are represented in the third chapter, where two different system configurations were tested. Firstly, the drift was measured for different transducer substrates, showing that the absence of the dielectric materials also removes the unwanted drift. In the second section, the measurements with the PI controller were shown, that showed unsatisfactory results even after system adjustments. The consequence was a reconfiguration of the measurement system to better accommodate the electrostatic drift effects. This new and modified system did not exhibit signs of electrostatic drift anymore. Nevertheless, the system still needed to be protected from ions. Thus, the measurements with a fixed bias

Die approbierte gedruckte Originalversion dieser Diplomarbeit ist an der TU Wien Bibliothek verfügbar
The approved original version of this thesis is available in print at TU Wien Bibliothek.
TU WIEN Bibliothek Your knowledge hub

voltage were conducted showing that the bias field did not cause unwanted instabilities or drift.

Outlook

Measuring the DC electric field with a high spatial resolution, low sensor cost and high reliability still remains a topic where further research is needed, though the active field sensors provide a good possible solutions for all these requirements. A constant bias voltage that shields from the ion-induced charge build-up on the dielectric materials surrounding the sensor shows promising results and should be further investigated and improved. Further things to investigate are temperature dependence, effects of humidity and how the system behaves when exposed to ion currents. Once these factors are known and can be controlled, the system can be calibrated and applied in real use cases.

Die approbierte gedruckte Originalversion dieser Diplomarbeit ist an der TU Wien Bibliothek verfügbar
The approved original version of this thesis is available in print at TU Wien Bibliothek.
TU Bibliothek Your knowledge hub WIEN

Bibliography

[1] R.G. Harrison. Fair weather atmospheric electricity. *Journal of Physics: Conference Series 301*, 2011.

[2] M.; Sadeghipoor H Razavipour, S.S.; Jahangiri. Electrical field around the overhead transmission lines. *Proc. World Acad. Sci. Eng. Technol.*, pages 568–571, 2012.

[3] Malcolm Sellars. *Electric Field Mill.* Master Thesis, University of Cape Town, 1995.

[4] David A. Hill et. al. *Electric Field Strength.* CRC Press LLC., 2000.

[5] Pengfei Yang et. al. A novel mems chip-based atmospheric electric field sensor for lightning hazard warning applications. *IEEE*, 2015.

[6] Mark N. Horenstein and Patrick R. Stone. A micro-aperture electrostatic field mill based on mems technology. *Journal of Electrostatics*, pages 515 – 521, 2001.

[7] George C. Underwood. *A MEMS Dual Vertical Electrometer and Electric Field-Mill.* Thesis, Air Force Institute of Technology Ohio, 2019.

[8] W.N. Cottingham and D.A. Greenwood. *Electricity and magnetism.* Cambridge University Press., 1991.

[9] Paul G Huray. *Foundations of Maxwell's Equations.* John Wiley & Sons, Inc., 1st edition, 2010.

[10] Robert L Coffie. *2D Electrostatic Fields: A Complex Variable Approach.* Milton: Taylor and Francis Group, 2021.

[11] Markus Hufschmid. *Grundlagen der Elektrotechnik: Einführung für Studierende der Ingenieur- und Naturwissenschaften.* Wiesbaden: Springer Fachmedien Wiesbaden, 2021.

[12] Silvan Schmid, Michael Lee Roukes, and Luis Guillermo Villanueva. *Fundamentals of Nanomechanical Resonators.* Springer, 2022.

[13] Franz Keplinger. *Sensorik Skriptum.* 2020.

[14] T. Priest, G. Scelsi, and G. Woolsey. Optical fiber sensor for electric field and electric charge using low-coherence, fabry–perot interferometry. *Applied optics, Jg. 36, Nr. 19*, page 4505–4508, 1997.

Die approbierte gedruckte Originalversion dieser Diplomarbeit ist an der TU Wien Bibliothek verfügbar
The approved original version of this thesis is available in print at TU Wien Bibliothek.
TU Bibliothek Your knowledge hub WIEN

[15] Andreas Kainz, H. Steiner, J. Schalko, A. Jachimowicz, F. Kohl, M. Stifter, R. Beigelbeck, F. Keplinger, and W. Hortschitz. Distortion-free measurement of electric field strength with a mems sensor. *Nat Electron*, pages 68 – 73, 2018.

[16] A. Kainz, F. Keplinger, and W. Hortschitz et. al. Noninvasive 3d field mapping of complex static electric fields. *Physical Review Letters 122*, 2019.

[17] Janaranjana Sampath Hiniduma Liyanage. *A Micromachined DC Electric Field Sensor Using a Torsional Micro Mirror*. Master Thesis, University of Manitoba, 2017.

[18] Roncin A. *Design of a Microelectromechanical Transducer for Electric Filed Measurement*. Master Thesis, University of Manitoba, 2004.

[19] Sampath Liyanage et. al. Torsional moving electric field sensor with modulated sensitivity and without reference ground. *Proceedings 350*, pages 568–571, 2017.

[20] K.B. Lee. *Principles of Microelectro Mechanical Systems*. John Wiley: New York, USA, 2011.

[21] Hajrudin Besic. *MEMS E-Field Sensor with Stabilized Optical Readout*. Thesis, TU Wien, 2020.

[22] Keithley a Tektronix company. *Low Level Measurements Handbook. Precision DC Current, Voltage, and Resistance Measurements*. Tektronix, 7th edition, 2013.

[23] Tao Chen et. al. Mems electric field sensor with biased electrically floating cover to measure electric field in ionic environments. *12th International Conference on Power, Energy and Electrical Engineering*, pages 175 – 179, 2022.

[24] Markus Demel. *Investigation of a MEMS Electric Field Sensor based on Alternating Charges*. Thesis, TU Wien, 2020.

Die approbierte gedruckte Originalversion dieser Diplomarbeit ist an der TU Wien Bibliothek verfügbar
The approved original version of this thesis is available in print at TU Wien Bibliothek.
TU WIEN Bibliothek Your knowledge hub